AGU PUBLICATIONS

Water Resources Research

RESEARCH ARTICLE

10.1002/2015WR017455

Key Points:

- Precipitation is investigated on global and monthly to centennial scales
- Macroweather precipitation space-time variability is characterized
- The space-time variability of three global precipitation products is compared

Correspondence to:
M. I. P. de Lima,
iplima@uc.pt

Citation:
de Lima, M. I. P., and S. Lovejoy (2015), Macroweather precipitation variability up to global and centennial scales, *Water Resour. Res.*, *51*, 9490–9513, doi:10.1002/2015WR017455.

Received 28 APR 2015
Accepted 4 NOV 2015
Accepted article online 6 NOV 2015
Published online 13 DEC 2015

© 2015. American Geophysical Union.
All Rights Reserved.

Macroweather precipitation variability up to global and centennial scales

M. I. P. de Lima[1,2] and S. Lovejoy[3]

[1]MARE - Marine and Environmental Sciences Centre, and IMAR-Institute of Marine Research, Coimbra, Portugal, [2]Department of Civil Engineering, University of Coimbra, Coimbra, Portugal, [3]Physics Department, McGill University, Montreal, Québec, Canada

Abstract We investigate precipitation variability in the "macroweather" regime—the intermediate regime between the familiar weather and climate regimes—which is associated to time scales from about 10 days to 30–100 years. Macroweather precipitation is characterized by negative fluctuation exponents. This implies—contrary to the weather regime—that fluctuations tend to cancel each other out, they diminish with time scale, this is important for seasonal, annual, and decadal forecasts. Aiming at a wide-scale range space-time statistical description of macroweather precipitation, we study the scaling of three centennial, global-scale precipitation products (one gauge based, one reanalysis based, and one satellite based) and systematically compare them over wide ranges of time and space scales. Although these products have very similar temporal statistics, at 5° resolution, they only agree with each other after being averaged over scales of several years, at scales larger than 2-3 decades, they disagree again. In space, there is less agreement on the statistics but—since the data have low resolutions (mostly 5° × 5°)—the disagreement is only over a small overall range of scales: the monthly data agree fairly well at scales 20°–30° and larger. Moreover, we quantify the outer scale limit of the temporal scaling (20–40 years, depending on the product, on the spatial scale, pixel, or global). Overall, results show that precipitation can be modeled with space-time scaling processes. The improved understanding of the space-time macroweather precipitation variability and the limitations of precipitation products provided by this work opens new perspectives to the stochastic modeling and forecasting of macroweather precipitation as well as separating natural and anthropogenic precipitation.

1. Introduction

A better understanding of atmospheric fields is needed to improve the modeling of different processes, not only in the atmosphere but also in systems that interact with it, namely the cryosphere, the geosphere, the hydrosphere, and the biosphere. Applications potentially range from global to regional and to local scales. Improved modeling also means a better ability to forecast at different scales and to develop more robust tools that can be used for assisting in conserving and managing natural resources, contributing to an overall improved understanding of the past, present, and future conditions on Earth.

In recent decades, numerous scaling analyses of precipitation and other atmospheric fields have clarified several aspects of atmospheric dynamics. In addition to the familiar weather and climate regimes, there is an additional intermediate macroweather regime. The three regimes alternate in their basic characters and, as explained below, this is a key for their understanding. For the temperature field, this three scaling regime picture is relatively clear, the macroweather regime spanning time scales from about 10 days to 30–100 years (in the industrial epoch, this upper limit is the lower figure, the preindustrial upper limit is not well established, see *Lovejoy* [2013] and *Lovejoy et al.* [2013a]). For precipitation, this picture is often not so clear, here we explore it further.

We start by noting the presence of a strong transition in the statistical properties of atmospheric fields at time scales τ_w of the order of 2–10 days, that was already recognized by *Van der Hoven* [1957], who theorized it as due to "migratory pressure systems of synoptic weather map scale. . ." followed by *Kolesnikov and Monin* [1965] and *Panofsky* [1969], who introduced the term "synoptic maximum." More recently, it has been attributed to baroclinic instabilities [*Vallis*, 2010]. On the other hand, *Lovejoy and Schertzer* [1986]

Table 1. A Comparison of Various Macroweather Precipitation Exponents: C_1 is the Codimension of the Mean, H is a Fluctuation Exponent, and β is the Spectral Exponent[a]

Reference	C_1	H	β	Data Analyzed
Ladoy et al. [1991]			0.3	Six 4 year segments of daily precipitation from Nîmes (France)
Tessier et al. [1996]	0.1 ± 0.05	-0.35[b]	0.1 ± 0.10	Thirty series from France, daily data averaged to monthly resolution; length, 10 years
de Lima [1998]			0.15, 0.17, 0.24	Respectively: 2 min data, 16 years; daily data, 32 years; monthly data, 59 years. Data are from Vale Formoso (Portugal), analyzed at 1 month and longer scales
Kantelhardt et al. [2006]	0.02 ± 0.01	-0.45 ± 0.06[c]	0.06 ± 0.12[d]	Ninety-nine series, daily precipitation analyzed from 2 days to decades. DFA[e] analysis
Lovejoy et al. [2012]	0.035	-0.42	0.08	From 11 × 13 point grid over the U.S., hourly precipitation over 29 years. Haar analysis

[a] These exponents are defined later in the text. We could also note an estimate by *Bunde et al.* [2005] using New Mexico paleoprecipitation from scales of years to over 2000 years: $H = -0.20$. The new analyses from Lovejoy and de Lima [2015] are discussed in the text.

[b] Inferred from the C_1, β estimate by using $\beta = 1 + 2H - K(2)$ and assuming $\alpha = 2$ so that $C_1 = K(2)/2$.

[c] The regression included a short part in the weather regime so that the exponent is a little too small.

[d] Inferred from C_1, H with $\alpha = 2$.

[e] Detrended Fluctuation Analysis.

stated "this is the minimum time scale of planetary structures." This interpretation was also recently strengthened and nuanced (τ_w as a typical lifetime) by *Lovejoy and Schertzer* [2010], who showed that the critical scale τ_w can be theoretically estimated from first principles if the (turbulent) Kolmorogov law held in the horizontal not only to scales comparable to the atmospheric-scale thickness ($\approx$10 km)—as is conventionally supposed—but up to planetary scales. This implies that the key dimensional quantity is the solar-induced energy rate density ($\approx 10^{-3}$ W/kg in the troposphere). Further evidence favorable to this theory, *Lovejoy and Schertzer* [2012a, 2013] confirmed that the spectrum of ocean (also turbulent up to planetary scales) could be analogously described since the energy rate density of surface currents is about 10^5 times smaller than atmospheric winds, implying (as observed) a transition at $\approx$1 year; the theory also successfully predicted the scaling structure of the Martian atmosphere (with a transition at about 1.8 days) [*Lovejoy et al.*, 2014]. Finally, (deterministic) numerical models well reproduce the weather and macroweather regimes including exponents in a realistic range, as do (stochastic) turbulence-based cascade models.

For precipitation, the transition scale τ_w between the high-frequency weather regime and the low-frequency macroweather regime varies somewhat with latitude from about 2–5 days, which is a little less than for the temperature (5–10 days) [*Lovejoy and Schertzer*, 2013, Figure 8.5c]. The overall statistical picture of precipitation variability is apparently qualitatively the same as for the temperature although for several reasons, it is less certain. These include: (a) the existence of high-quality paleotemperature data (but absence of comparable paleoprecipitation data) that allow us to estimate the temperature statistics at decadal and centennial scales for both preindustrial and industrial epochs; (b) the temperatures are not too intermittent so that the statistics are more robust; (c) the theoretical and GCM modeling implications of anthropogenic effects on the temperature are more straightforward than for precipitation.

The vast majority of temporal precipitation scaling analyses have been in the weather rather than macroweather regime [e.g., *Olsson and Niemczynowicz*, 1996; *Pathirana et al.*, 2003; *Garcia-Marin et al.*, 2008; *de Lima and de Lima*, 2009; *Sun and Barros*, 2010; *Rysman et al.*, 2013; M. Nogueira and A. P. Barros, Dynamical downscaling of quantitative precipitation estimation for hydrological predictions in the Southern Appalachians, submitted to *Journal of Hydrology*, 2015], although some provided estimates in both regimes: *Ladoy et al.* [1991], *Tessier et al.* [1996], *de Lima* [1998], and *Lovejoy et al.* [2012]. For comparison, Table 1 shows the (limited) number of macroweather exponents published to date; we discuss them in detail below. We could also mention studies of clustering and extremes of macroweather precipitation that are also in a theoretical scaling framework [e.g., *Bunde et al.*, 2005, 2013].

One reason for the relative paucity of temporal macroweather precipitation analyses is the difficulty in clearly identifying the transition scale τ_w. For example, transitions from zero to finite rain rates lead to breaks in the scaling and it is still not clear how much of this effect is due to instrumental issues at low rain rates, and how much is due to true transitions from rain to no-rain (see the debate in *Lovejoy et al.* [2008], *de Montera et al*. [2009], *Verrier et al*. [2010, 2011], *Hoang et al*. [2012], and *Gires et al*. [2013] and the review in *Lovejoy and Schertzer* [2013, Chapter 4]).

Technical issues concerning different data analysis techniques have also contributed to lack of clarity on macroweather precipitation. For example, the trace moment technique often used to analyze the (strong) intermittent component of precipitation involves a nonlinear transformation of variables at the smallest scales (the estimation of the relevant driving fluxes, using for example, absolute first differences). In order to use it to obtain macroweather regime estimates, the data must first be averaged over macroweather scales before the flux is estimated; in many publications, this was not done (see however *Lovejoy and de Lima* [2015], referred to below as LdL). The application of the Detrended Fluctuation Analysis (DFA) technique on daily precipitation data [*Kantelhardt et al*., 2006] also has some issues (Table 1). The DFA loses a factor of 2 at the high frequencies so that the analyses of daily data start at 2 days: as a consequence, when regressions were made, the weather regime was mixed in with the macroweather regime leading to biases in the exponents. In addition, we could mention that the DFA is usually applied to the running sum of the data rather than to the data itself; this not only increases the exponents by one (this is easy to deal with), but it also makes scale breaks harder to detect.

From Table 1, it can also be seen that the focus of temporal macroweather scaling statistics has been from single station data so that a clear global picture cannot easily be painted. At the empirical level, we need clarification of (a) the (possible) variation of the exponents with latitude, (b) the variation over land and over ocean, (c) the global-scale averaged values, (d) the expected anthropogenic (low frequency) effects, (e) the degree of agreement/disagreement between different techniques for estimating areal precipitation, and (f) the space-time macroweather statistics. Although the temporal statistics are in many ways deficient, at least several have been published. In contrast, there have been no studies of spatial macroweather variability whatsoever—these need gridded weekly or monthly averaged precipitation fields of the type used below.

This paper focuses on these and the related theoretical issues. We investigate the temporal and spatial precipitation statistics of climatological precipitation products, and compare their statistical variabilities in time and space; moreover, we also explore several local, particularly long gauge precipitation time series. We quantify the outer scale macroweather limit where the temporal scaling breaks down (τ_c). In particular, the empirical investigation of macroweather precipitation carried out here envisaged a theoretical framework for modeling precipitation over the relevant range of scales. A companion paper (LdL) considers the joint space-time properties and directly analyses the spatial cascade structure using trace moments.

The argument by *Lovejoy and Schertzer* [2010, 2013] that space-time turbulent cascade models (the Fractionally Integrated Flux; FIF model), that were developed for weather scales, could be extended to the macroweather regime (the "extended FIF"; EFIF) simply by allowing the cascades to develop starting from an (outer) time scale much longer than τ_w, leads to the conclusion that space-time macroweather statistics should—at least approximately—satisfy a basic space-time statistical factorization property which is a theoretical constraint for models. This stochastic forecasting of macroweather precipitation as well as a new space-time macroweather precipitation model—the ScaLIng Macroweather Model (SLIMM)—is discussed in detail in LdL.

2. The Data

To investigate the space-time structure of precipitation in time, over scales from about 1 month to centuries (or longer), and in space, from global scales down to scales of a few degrees (or less), we explored three centennial, global-scale precipitation products: one instrument based, one reanalysis based, and one satellite and gauge based. These products allow us to study precipitation over land, ocean, and the globe. Table 2 gives basic information on these products that we further detail below.

The Global Historical Climatology Network (GHCN) precipitation product [*Vose et al*., 1992]—GHCN-Monthly version 2, updated through 2012 and available from the NOAA site—is the most important gauge-based data set: it consists of monthly data for the period 1900–2012, at 5° × 5° resolution. Note that only the precipitation anomalies were reported (i.e., with the annual cycle removed and relative to the 1961–1990 reference period), which lessens concerns about missing data, series consistency, etc. The GHCN product being gauge based, it is thus also land based (i.e., restricted to land; but this product is not only missing data over ocean, it

Table 2. Summary of the Main Characteristics of the Three Global Precipitation Products, All at Monthly Resolution: the Global Historical Climatology Network (GHCN), the Twentieth Century Reanalysis (20CR), and the *Smith et al.* [2012] Satellite/Gauge Reconstruction ("Smith")[a]

Product	GHCN	20CR	Smith
Type	Gridded stations	Reanalysis	Satellite/station hybrid
Reference	*Vose et al.* [1992]	*Compo et al.* [2011]	*Smith et al.* [2012]
Period covered	1900–2012	1871–2012	1900–2012
Spatial resolution	5° × 5°	1.875° × 1.875°	5° × 5°
Data type	Anomalies	Raw rain rates	Raw rain rates

[a] The 20CR and Smith data were complete whereas the GHCN data were quite incomplete: for example, the fraction of the pixels with data were 14%, 31%, and 18% in 1900, 1990, and 2012, respectively.

is often also missing data over land: virtually all the pixels have significant outages, see Table 2). Since it does not include the oceans, which comprise 70% of the Earth's surface, it will likely give a biased view of global-scale precipitation. Indeed, we examine this below, it is likely that oceanic precipitation has different statistical characteristics than precipitation over land, and (since most of the heating is of the ocean) this includes a potentially much stronger response to anthropogenic warming. Historically, the GHCN and the Global Precipitation Climatology Centre (GPCC—Global Monitoring Product version 4) [see *Becker et al.*, 2013] products have been similar on an annual basis, though GHCN has higher interannual variability due to its smaller network [*Vose et al.*, 2014]; because of this similarity, we did not analyze the GPCC product.

Regarding ocean precipitation, the only two relevant data sets are from the Twentieth Century Reanalysis (20CR) [*Compo et al.*, 2011] and the *Smith et al.* [2012] satellite/gauge reconstruction (hereafter abbreviated "Smith"), but both of these products are quite indirect:

a. The 20CR data (at 2° × 2° and 6 h resolution) are derived solely from surface pressure data and monthly Sea Surface Temperature (SST) data: the precipitation is entirely inferred from a numerical model, the result—a "reanalysis"—being a kind of data/model hybrid; the derived product used here is monthly at 1.875° resolution. However, when pertinent for comparing this product with the other precipitation products, the data were degraded spatially as appropriate.
b. The Smith data use a gauge calibrated Infrared (IR) satellite rain algorithm to infer global-scale rain over the satellite observation period 1979–2012. This is then used to calculate Empirical Orthogonal Functions (EOFs). Finally, in the presatellite era, the historic land-based gauge data (GHCN) are used to estimate the coefficients of each EOF, yielding global-scale estimates at 5° × 5°, monthly resolution. The Smith product uses the base data of the Global Precipitation Climatology Project (GPCP, version 2.1) [see *Adler et al.*, 2003]—merged satellite and gauge analysis—for the reconstruction of historical precipitation, it supersedes the GPCP.

Let us now compare the temporal variability of the global-scale averages of the different precipitation products (GHCN, 20CR, and Smith). Figure 1 shows the annual precipitation rate anomalies averaged over land only, ocean only, and globally. The product that spans the longest period is the 20CR 1871-2012, we analyzed the period, 1880–2004. The main thing that eye catches in Figure 1 is that it shows differences between the products at the highest resolution: in particular, notice that the gauge-based product (GHCN) is much more variable than the Smith product, itself more variable than the 20CR product. We can also note that while there is some overall agreement at the lowest frequencies, the higher frequencies are often in disagreement. We show in the following sections that the study of Haar fluctuations extends the analysis to all scales.

Table 3 shows the global-scale raw rain rate averages obtained from the 20CR and Smith data; results are not shown for the GHCN product because it only gives anomalies. We can see that there is a disagreement of ≈20% for the land estimates, but only about 5% for the ocean estimates: overall, the disagreement is about a 10% for the global estimates.

It is to be expected that the use of spatial interpolation/averaging techniques to obtain gridded data as well as the different characteristics of the models/instruments have influence on the relative behaviors in the different precipitation products. More details on the agreement/disagreement between these products are given in the next sections.

We have also used gauge data to assess the temporal statistics of local precipitation: 15 near-complete and exceptionally long monthly precipitation series from Portugal. The data set comprises records from 12

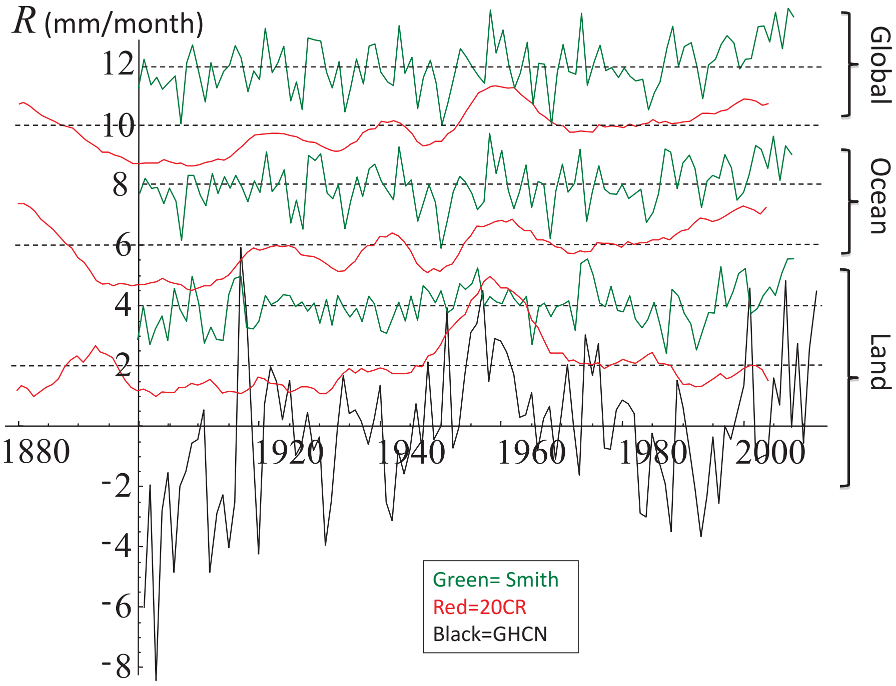

Figure 1. The annual precipitation rate anomalies averaged over (bottom) land only, (middle) ocean, and (top) globally. The black curve is for the Global Historical Precipitation network (GHCN) from January 1900 to December 2012. The red curves are for the Twentieth Century Reanalysis (20CR) from 1880 to 2004, and the green curves are for the *Smith et al.* [2012] satellite/gauge reconstruction (abbreviated "Smith"). The GHCN and Smith products were at 5° × 5° resolution, the 20CR data were at 1.875° resolution. The data were shifted upward by 2 mm/month increments as indicated by the dashed horizontal lines. Reproduced from *Lovejoy and de Lima* [2015].

meteorological stations scattered over mainland Portugal (between latitudes 36°56′N and 42°09′N and longitudes 6°10′W and 9°34′W, south-western Europe) and 3 stations from the Portuguese North Atlantic Islands of Madeira and Azores (Madeira, 32°38′N, 16°53′W; Azores, centered 38°35′N, 28°05′W). Some of the time series date back to the nineteenth century, spanning periods that range between 98 and 148 years. The oldest records are from 1863, the end date is 2010 for all series. In mainland Portugal, precipitation shows high interannual variability and marked seasonality; there are strong north-south and east-west precipitation gradients: the climate is greatly influenced by the latitude, the orography, and the proximity of the Atlantic Ocean. In the Madeira Island, the complex topography of the island and its small size play a crucial role in the local precipitation regime that is marked by high spatial variability. In the Azores, located in the North Atlantic ridge, the warm Gulf Stream and their latitudinal position affect the islands' climatic conditions; for most of the year, the Atlantic depressions track across the Azores Islands.

3. Methodology: Exploring Temporal and Spatial Macroweather Precipitation

3.1. Temporal Statistics

3.1.1. The Different Character of Weather, Macroweather, and Climate Regimes

The different characters of the three scaling regimes (weather, macroweather, and climate regimes, from high to low frequencies) can be characterized using scaling exponents. Let us consider the temporal fluctuations in an atmospheric variable I over an interval Δt as $\Delta I(\Delta t)$; then, in a scaling regime, the mean fluctuations vary with scale as $<\Delta I(\Delta t)>\approx \Delta t^{H}$, where H is the fluctuation exponent and "$< >$" indicates statistical averaging. For Gaussian processes, it is equal to the Hurst exponent; the definition used here is more general; so that it can apply to general—multifractal—processes. While in the weather and climate regimes, mean fluctuations tend to grow with scale ($H>0$), they appear

Table 3. Average Precipitation Rates for the Last Century Over Land, Ocean, and Globe, Obtained From the 20CR and the Smith Product[a]

Product	Land	Ocean	Global
Smith	67.9	87.9	81.7
20CR	85.6	93.9	91.3

[a] All entries are in mm/month. Note that the Smith product yields smaller values, but the general trend is the same for both products.

unstable, in the macroweather regime, they decrease ($H<0$), they appear stable. In the latter regime, since $H<0$, mean fluctuations tend to cancel out so that averages over longer and longer times increasingly converge. However (at least for the temperature, but probably also for the precipitation and other atmospheric fields), rather than converging to a fixed "climate" as one might expect, after about 10–30 years (industrial period) and ≈100 years (preindustrial period), there is a transition to another scaling regime—the climate proper—with again $H>0$ (as in the high-frequency weather regime) and with fluctuations growing with scale. A recent analysis using paleotemperatures [*Lovejoy*, 2014b] finds that this alternation continues through two larger-scale (macroclimate, megaclimate) regimes, out to time scales of over 500 Myr. We could note that, for Gaussian processes (fractional Brownian motion, fBm), the distinction $1/2< H>1/2<1$ or $0<H<1/2$ is often made between "persistent" and "antipersistent" processes, which for Gaussian processes refers to correlations between successive increments of the process. But this is not relevant in the more general (non-Gaussian) case considered here and in no way contradicts our more basic and general distinction between $H<0$ and $H>0$.

In the next sections, we discuss how to define and statistically quantify the fluctuations as functions of scale, give the results of the data analysis, and discuss the implications for precipitation modeling.

3.1.2. Quantifying the Variability Over Scales: Fluctuations, Structure Functions

The mean and the root-mean-square (RMS) fluctuations can be used to quantify the high and low-frequency variability in precipitation. In this paper, we use Haar fluctuations [see *Lovejoy and Schertzer*, 2012b], which have numerous advantages: they are simple to understand, to estimate, and to interpret and are useful for most geofields over huge ranges in space and time (i.e., $-1<H<1$; see below). The Haar fluctuation of the precipitation R at time scale Δt is simply the difference of the mean of R over the first and second halves of the interval Δt:

$$(\Delta R(\Delta t))_{Haar}=\frac{2}{\Delta t}\int_{t+\Delta t/2}^{t+\Delta t} R'(t')dt'-\frac{2}{\Delta t}\int_{t}^{t+\Delta t/2} R'(t')dt' \tag{1}$$

where we have added the subscript "Haar" to distinguish it from other common definitions of fluctuation (below); moreover, we have suppressed the t dependence because we will assume that the fluctuations are statistically stationary. With an appropriate "calibration" constant (a "canonical" factor 2 is used throughout this paper), in scale regions where $H>0$, the Haar fluctuations are nearly equal to the differences, whereas in scale regions where $H<0$, they are nearly equal to the anomalies:

$$\begin{gathered}(\Delta R(\Delta t))_{dif}=R(t+\Delta t)-R(t)\\ (\Delta R(\Delta t))_{anom}=\frac{1}{\Delta t}\int_{t}^{t+\Delta t} R'(t')dt';\;\; R'=R-\overline{R}\end{gathered} \tag{2}$$

where $\overline{R}$ is the mean over the entire series. The reason for these relations between the different fluctuations is that the Haar fluctuation is equal to the difference fluctuation of the anomaly fluctuation or alternatively it is equal to the anomaly fluctuation of the difference fluctuation (they commute), see *Lovejoy and Schertzer* [2012b].

The simplest way to characterize the fluctuations is through (generalized) structure functions: $\langle \Delta R(\Delta t)^q\rangle$, where "<.>"indicates statistical (ensemble) averaging; the term "generalized" is used to indicate the use of fluctuations other than the usual differences, and moments of order q other than the usual value 2.

Physically, if the system is scaling, then the fluctuations are related to the driving flux φ by:

$$\Delta R(\Delta t)=\varphi_{\Delta t}\Delta t^H \tag{3}$$

where the subscript "Δt" is used on φ to indicate that it is the flux at resolution Δt. The structure function $S_q(\Delta t)$ is:

$$S_q(\Delta t)=\langle \Delta R(\Delta t)^q\rangle=\langle \varphi_{\Delta t}^q\rangle \Delta t^{qH} \tag{4}$$

Turbulent fluxes are conserved from scale to scale so that $\langle\varphi_{\Delta t}\rangle$=constant (independent of scale, Δt); this implies that $\langle \Delta R\rangle \propto \Delta t^H$ so that H is the mean fluctuation exponent.

Beyond the simplicity of interpretation, the Haar fluctuations give a good characterization of the variablity for stochastic processes with $-1<H<1$. In contrast, fluctuations defined as differences or as anomalies only usefully characterize the variations with scale over the narrower ranges $0<H<1$ and $-1<H<0$, respectively [see *Lovejoy and Schertzer*, 2012b; *Lovejoy et al.*, 2013b]. Outside these ranges in H, the fluctuation at scale Δt is no longer dominated by frequencies $\approx \Delta t^{-1}$ so that the fluctuations depend spuriously on details of the finite data sample; specifically, they depend on either the highest or the lowest frequencies that happen to be present.

The generic scaling process is multifractal; so, in general, φ has statistics:

$$\langle \varphi_{\Delta t}^{q} \rangle \propto \Delta t^{-K(q)} \tag{5}$$

where $K(q)$ is a scaling, convex exponent function. Substituting (5) into (4), we obtain:

$$S_q(\Delta t)= \langle \Delta R(\Delta t)^q \rangle \propto \Delta t^{\xi(q)};\;\; \xi(q)=qH-K(q) \tag{6}$$

where $\xi(q)$ is the "structure function exponent." For the moment, note again that the mean ($q=1$) flux $<\varphi_{\Delta t}>$ is independent of Δt (see above), so that $K(1)=0$; hence, $\xi(1)=H$. Note also that for quasi-Gaussian processes, none of the moments of $\varphi_{\Delta t}$ have any scale dependence so that $K(q)=0$ and $\xi(q)=qH$, which means that, for these, all the scale dependence is characterized by H. The basic stochastic process that reproduces the statistics (equation (6)) is the Fractionally Integrated Flux model [*Schertzer and Lovejoy*, 1987].

Finally, the RMS fluctuation $\langle \Delta R(\Delta t)^2 \rangle^{1/2}$, denoted simply $S(\Delta t)$ to lighten the notation, has exponent $\xi(2)/2$ so that the error in using the quasi-Gaussian approximation for the variance (i.e., $\xi(2)/2 = H$) is $\xi(2)/2 - H = K(2)/2$. In the temporal domain, the latter is typically small (in the range 0.02–0.04) so that the approximation $\xi(2)/2 \approx H$ is fairly accurate. But in the spatial domain, the same does not apply and this approximation is poor; in section 5, we show that in the spatial domain, the difference $\xi(2)/2 - H$ can be readily in the range 0.1–0.2, and that further characterization is needed. Below, we will use S to denote the RMS Haar fluctuatiońs structure functions. For clarity, when needed, we sometimes use the subscript t, x to denote time and space variables, functions.

As a practical matter, for individual series, for each lag Δt, fluctuations are estimated for all the disjoint intervals of length Δt that are used. In cases where there are many series (i.e., one for each spatial grid point), we make an assumption about statistical spatial homogeneity so that the statistics at each grid point is assumed to be the same (that does *not* mean they are assumed to be statistically independent!), so that for each Δt, fluctuations are taken over all the disjoint intervals in time and over all the grid points.

3.1.3. The Uncertainty in $S(\Delta t)$

Let us briefly discuss the uncertainty with which $S(\Delta t)$ $(=S_2(\Delta t)^{1/2})$ is estimated, i.e., the deviations of the estimated $S(\Delta t)$ from its true value. There are several sources of uncertainty to consider. The most problematic are the systematic uncertainties associated with scientific errors in the reconstructions and in the formulation of the models.

Let us first consider uncertainties due to measurement errors and uncertainties arising from limited sample sizes. These are the classical sources of uncertainty: in deterministic theoretical frameworks in which the series $R(t)$ are considered deterministic, only the errors are stochastic. Measurement error is the easiest to deal with. Recall that for each Δt, the corresponding $S(\Delta t)$ is the actual average fluctuation over all the corresponding intervals of the series (to simplify the discussion, we will consider a pure, single time series). For the series studied here, the contribution of the classical measurement error—i.e., a white noise or short range correlated noise such as an Auto Regressive order one (AR(1)) process noise—to the uncertainties is quite small. We can be confident of this since if such a measurement error dominated the signal over any range (presumably at small Δt), then over that range, $S(\Delta t)$ would decay as the characteristic white noise fall-off $\Delta t^{-1/2}$ (i.e., with a slope $-1/2$ on log-log plots); yet in the analyses presented here, there is no evidence for such regimes, and we conclude that this is not an important source of uncertainty.

However, for each Δt, there will be errors in $S(\Delta t)$ due to inadequate sampling. This arises from the fact that we have a finite segment of a single stochastic realization of the precipitation process. Since for a given Δt, the number of disjoint intervals used to estimate $S(\Delta t)$ varies inversely with the interval width, the uncertainty will be larger at large Δt than at small Δt. If the intervals were statistically independent of each other, then classically, the standard deviation of the estimated $S(\Delta t)$ values due to poor sampling would increase as $\Delta t^{-1/2}$. However, since empirically $S(\Delta t)$ does not falloff with $\Delta t^{-1/2}$, on the contrary, the process has long range statistical dependencies, so that the standard theory (that supposes statistical independence) will not apply. The only practical way to estimate this uncertainty is to construct an explicit stochastic model using a bootstrap procedure wherein the model and optimal parameters are estimated from the (single, finite) realization and then obtain uncertainties estimates from numerical simulations. However, it is not the aim of this paper and thus it has not been done here.

Finally, there is the less familiar stochastic uncertainty that is more difficult to deal with, especially in the presence of statistical long range dependencies. In our case, stochastic uncertainty refers to the fact that we are dealing with a single space-time realization of the atmosphere (the Earth's atmosphere over roughly the last century), yet we are attempting to estimate statistics (exponents) of a stochastic space-time macroweather process. The difficulty is underlined since scaling is a symmetry that is only exactly respected on an (infinite) statistical ensemble and we only have access to a single realization.

Clearly, such stochastic uncertainty needs to be investigated with stochastic models. For volcanism, this was done, for example, in *Lovejoy* [2014b]: four simulated multifractal volcanic forcing series from the same statistical ensemble were produced differing substantially from each other (as one would expect for four different millennial volcanic series). The realization to realization variations in the estimated $S(\Delta t)$ were then determined, notably for subseries of various lengths. But what does such a stochastic uncertainty analysis tell us? In the case of simulated volcanic reconstructions mentioned above, it is best viewed as the variability in volcanism over epochs separated by large time intervals: it is really the epoch to epoch variability in the signal (although the sampling characteristics were also studied). The interpretation of stochastic uncertainty in scaling processes with long range dependencies is thus rather different from the uncertainties with which we are more familiar.

3.1.4. Comparing the Precipitation Products at Different Time Scales

Although there are many ways of estimating areal precipitation, these are all indirect, involving various assumptions. While this may be obvious for radar (which measures reflectivity, not rain rate), it is also true for instrumentally based products such as the GHCN or the CPC (Climate Prediction Center; see more details below) gridded precipitation products. In the latter case, the difficulties are due to large amounts of missing data: "holes" at all scales, the data collection sites themselves are typically fractal (scaling), e.g., *Lovejoy et al.* [1986], *Korvin et al.* [1990], *Nicolis* [1993], *Giordano et al.* [1995], *Doswell and Lasher-Trapp* [1997], and *Mazzarella and Tranfaglia* [2000], and see also the discussion in *Lovejoy and Schertzer* [2013]. The result is that all estimates of global-scale precipitation involve nontrivial assumptions leading to different products. While this is also true of the standard atmospheric variables of state, it is especially true of precipitation which has a huge variability combined with nontrivial measurement issues, notably for low and zero rain rates, and extreme high rain rates (depending somewhat on the estimation technique). We thus anticipate that the three precipitation data sets analyzed here will be quite different since they are of qualitatively different natures: a gridded instrumental product (GHCN), an indirect instrumental/model product (20CR) and an indirect (gauge, satellite) instrumental product (Smith).

The only way to gain confidence in the quality and accuracy of any of the products is to systematically compare them as functions of space and time scale. Such an evaluation is important because even if they are significantly different at high resolution, we may expect them to become more and more similar with increasing space-time averaging scales, and their agreement/disagreement will shed light on their intrinsic limitations.

Consider two precipitation products $R_1(t)$ and $R_2(t)$. The simplest way to study their similitude is to consider the differences: $\delta R(t) = R_1(t) - R_2(t)$; these can then be directly investigated by considering their Haar fluctuations, $\Delta\delta R(\Delta t)$. At the scale Δt, denote the series with the largest variance by R_1: $\langle \Delta R_1(\Delta t)^2 \rangle \geq \langle \Delta R_2(\Delta t)^2 \rangle$ (i.e., $\langle \Delta R_1(\Delta t)^2 \rangle = \max\left[\langle \Delta R_1(\Delta t)^2 \rangle, \langle \Delta R_2(\Delta t)^2 \rangle\right]$). Consider the extreme cases of two identical series ($R_1 = R_2$; hence, $\Delta\delta R(\Delta t) = 0$), and of two series identical but with opposite signs ($R_1 = -R_2$; hence, $\Delta\delta R(\Delta t) = 2\Delta R_1(\Delta t)$). These cases are the extremes of positive and negative correlations:

$$\begin{aligned} \langle \Delta\delta R(\Delta t)^2 \rangle &= 0; \qquad R_1 = R_2 \\ \langle \Delta\delta R(\Delta t)^2 \rangle &= 4\langle \Delta R_1(\Delta t)^2 \rangle; \quad R_1 = -R_2 \end{aligned} \tag{7}$$

Finally, consider the case of two statistically independent series:

$$\langle \Delta\delta R(\Delta t)^2 \rangle = \langle \Delta R_1(\Delta t)^2 \rangle + \langle \Delta R_2(\Delta t)^2 \rangle \leq 2\langle \Delta R_1(\Delta t)^2 \rangle \tag{8}$$

Combining these results, we see that for positively correlated series:

$$\langle \Delta\delta R(\Delta t)^2\rangle^{1/2} \le \sqrt{2}\max\left[\langle \Delta R_1(\Delta t)^2\rangle^{1/2}, \langle \Delta R_2(\Delta t)^2\rangle^{1/2}\right] \tag{9}$$

This will presumably be the range of interest for two products supposedly representing the same rain fields. For reference, for positively or negatively correlated series, we have:

$$\sqrt{2}\max\left[\langle \Delta R_1(\Delta t)^2\rangle^{1/2}, \langle \Delta R_2(\Delta t)^2\rangle^{1/2}\right] \le \langle \Delta\delta R(\Delta t)^2\rangle^{1/2} \le 2\max\left[\langle \Delta R_1(\Delta t)^2\rangle^{1/2}, \langle \Delta R_2(\Delta t)^2\rangle^{1/2}\right] \tag{10}$$

3.2. Spatial Fluctuation Statistics

Before considering the spatial variability, we must discuss a complication arising in connection with anomalies that was absent in the analysis of temporal fluctuations. Recall that station data are usually used to estimate anomalies since this allows for the detection and elimination of many systematic errors; for the GHCN product, these were the only data that were available. However, for the 20CR and Smith products, we are supplied with the absolute rain rates. From these, the first step in calculating the anomalies is to remove the annual cycle for each spatial location (pixel) $\underline{r}$. Let us call this field (with only annual detrending) the "raw" precipitation rate $R(\underline{r}, t)$ at location $\underline{r}$. The anomalies $R_{anom}(\underline{r},t)$ are then determined by subtracting the location's long-term time average $\overline{R}(\underline{r})$:

$$R_{anom}(\underline{r}, t) = R(\underline{r}, t) - \overline{R}(\underline{r}) \tag{11}$$

Conventionally, $\overline{R}(\underline{r})$ is given by 30 year averages (for the GHCN, 1961–1990); here for the 20CR and Smith data, we used the averages over their full lengths (otherwise we artificially introduce a time scale of 30 years).

For the temporal fluctuations, we have:

$$\begin{aligned} \Delta R(\underline{r}, \Delta t) &= \frac{2}{\Delta t}\int_{t+\Delta t/2}^{t+\Delta t} R(\underline{r}, t')dt' - \frac{2}{\Delta t}\int_{t}^{t+\Delta t/2} R(\underline{r}, t')dt' \\ &= \frac{2}{\Delta t}\int_{t+\Delta t/2}^{t+\Delta t} \left(R_{anom}(\underline{r}, t') + \overline{R}(\underline{r})\right)dt' - \frac{2}{\Delta t}\int_{t}^{t+\Delta t/2} \left(R_{anom}(\underline{r}, t') + \overline{R}(\underline{r})\right)dt' \\ &= \Delta R_{anom}(\underline{r}, \Delta t) \end{aligned} \tag{12}$$

This shows that the raw and anomaly temporal fluctuations are the same, and that is why we ignore the distinction in section 4, on temporal variability. However, for the spatial fluctuations, we have:

$$\begin{aligned} \Delta R(\Delta r, t) &= \frac{2}{\Delta r}\int_{r+\Delta r/2}^{r+\Delta r} R(r', t)dr' - \frac{2}{\Delta r}\int_{r}^{r+\Delta r/2} R(r', t)dr' \\ &= \frac{2}{\Delta r}\int_{r+\Delta r/2}^{r+\Delta r} \left(R_{anom}(r', t) + \overline{R}(r')\right)dr' - \frac{2}{\Delta r}\int_{r}^{r+\Delta r/2} \left(R_{anom}(r', t) + \overline{R}(r')\right)dr' \\ &= \Delta R_{anom}(\Delta r, t) + \Delta\overline{R}(\Delta r) \end{aligned} \tag{13}$$

Therefore, for the spatial fluctuations, it is important to distinguish the statistics of $\Delta R(\Delta r,t)$ ("raw") and $\Delta R_{anom}(\Delta r,t)$ (in the above, for simplicity, we have reduced the vector position dependence to a scalar one: below r and Δr will only be taken as zonal or meridional coordinates and coordinate differences, respectively).

4. Temporal Macroweather Precipitation Fluctuations and Variability

4.1. The Temporal Variability of the Precipitation Products

Figure 2a shows the first-order ($q = 1$) structure functions (the mean absolute Haar fluctuation) for monthly precipitation data from the GHCN and 20CR products (the different curves correspond to different subproducts and are explained in the caption of Figure 2a). This figure shows also the structure function of the 20CR reanalysis data at 45°N (6 h, 2° resolution, from 1871 to 2008) and, complementary, the corresponding structure function of the Climate Prediction Center (CPC, hourly resolution) gauges (continental U.S., some of the CPC data were also incorporated into the GHCN product); the curves for the CPC data are from *Lovejoy et al.*

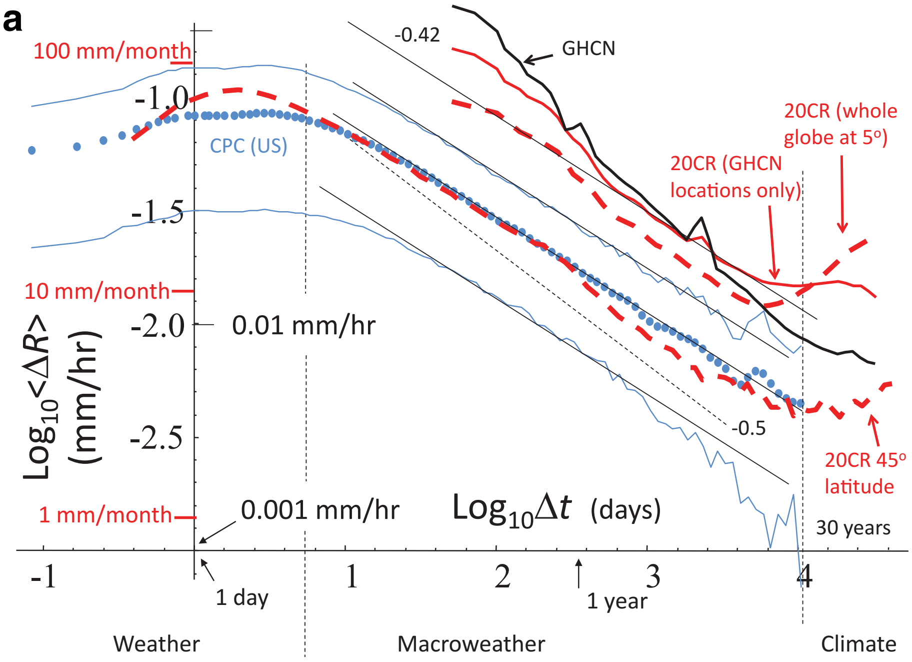

Figure 2. (a) *Upper right curves*: the temporal RMS Haar structure functions for the 20CR and GHCN precipitation products at 5° × 5° pixel scale. The original (1.875° × 1.875°) 20CR data were first converted into anomalies by subtracting the long-term mean of the annually detrended data. The monthly 20CR product was degraded to the same 5° × 5° grid of the GHCN product. The pixel-scale GHCN curve is shown (black) along with the 20CR curves ensemble averaged over all the pixels (with map factors, the *whole globe* average: red, short dashed curve), and only over the same pixels as the GHCN data (*land*: red, short solid curve). *Lower curves*: the first-order (*not* RMS) structure function (the mean absolute Haar fluctuation) using precipitation data from the Climate Prediction Center (CPC, continental U.S.) gauges (blue dots) as well as the corresponding structure function of the 20CR reanalysis at 45°N (6 h, 2° resolution, from 1871 to 2008, red, long dashed curve). ΔR is the mean absolute fluctuation in the rain rate over a time interval Δt. For the CPC product, we also show the corresponding one-standard-deviation limits (thin, blue) with reference lines slopes $H = -0.42$ (solid black lines) and -0.5 (dashed black line, corresponding to a Gaussian white noise process). The one-standard-deviation limits are calculated from the ensemble of Δt scale fluctuations for each grid point, for each Δt, it quantifies how much the amplitude of the fluctuations varies from one grid point to another. These curves are from *Lovejoy et al.* [2012]. b. The pixel-scale world maps of the distribution of H_t for monthly precipitation for the three data sets discussed in the paper (5° × 5°, 3.75° × 3.75°, and 5° × 5° resolutions for GHCN, 20CR, Smith data sets, respectively, top to bottom; the 20CR resolution was degraded 2 × 2 pixels so as to be more comparable to the resolutions of the other data sets). The transition from reddish to bluish occurs at roughly the mean H_t value of -0.4. The exponents were estimated from the annually detrended data using the Haar analysis technique with exponents fit over the range 6 months to 12 years (to avoid possible biases at low frequencies due to anthropogenic effects or poor statistics). The pink in the GHCN map corresponds to no data (mostly oceans). Reproduced from *Lovejoy and de Lima* [2015].

[2012]. NOAA's CPC product is unique in its high temporal resolution over a large number of contiguous grid points. The product analyzed was a (near complete) subset of the CPC data for the 29 years 1948–1976 (at this date there is a data gap of several weeks so that we did not extend the analysis to more recent times). The CPC data were gridded on 2.5° × 2.0° boxes by using a modified Cressman scheme (an interpolation technique); its central rectangular 13 × 21 point region was used: from −122.5° to −72.5° longitude (every 2.5° ≈ 210 km at these latitudes) and from 30° to 54° latitude (every 2° ≈ 220 km). Each grid box had a near-complete ≈257,000 hourly series.

The different statistical regimes emerge in Figure 2a; in particular, note the weather regime approximately at scales $\Delta t < 2$ days and see the rise beyond ≈30 years (in particular, for the 20CR data): the transition from macroweather to the climate. The macroweather scaling exponent parameter estimated for the CPC data, $H = -0.42$, is higher than the value -0.5 corresponding to a Gaussian white noise process (see the reference lines in Figure 2a). The RMS pixel-scale Haar fluctuations are also shown for comparison; they are mostly shifted up due to the difference between the $q = 1$ and RMS amplitudes.

The analysis of the ratio of the mean $q = 1$ and RMS fluctuations (i.e., using $\langle \Delta R(\Delta t)\rangle / \langle \Delta R^2(\Delta t)\rangle^{1/2} \approx \Delta t^{K(2)/2}$) for the CPC data set confirms the transition from high intermittency behavior at scales less than a few days (the "weather regime," $K(2)/2 \approx 0.35$, with $K(2)/2$ used as an approximation to C_1—the intermittency coefficient) to low but not insignificant intermittency behavior at scales of months to years (the "macroweather regime,"

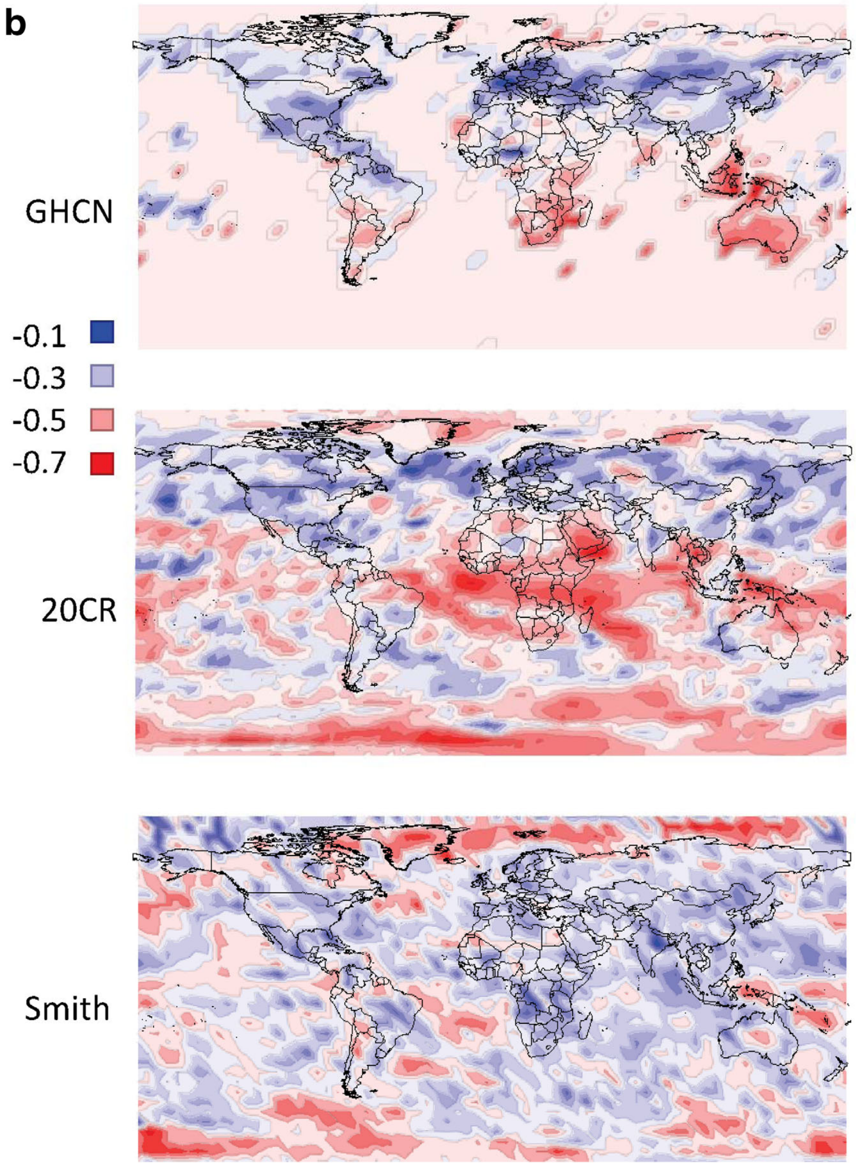

Figure 2. (continued)

$K(2)/2 \approx 0.035$, see *Lovejoy et al.* [2012] and LdL for a comparison of the weather and macroweather statistics). The use of the second moment is conventional since it directly determines the exponent β of the spectrum $E(\omega) \approx \omega^{-\beta}$, where ω is the frequency: $\beta = 1 + \xi(2)$; we therefore have used the RMS statistics below. However, in section 5, we see that in the spatial macroweather domain $K(2)/2 \approx 0.1$ so that the approximation $\xi(2)/2 \approx H$ is poor, and a full multifractal characterization is needed (i.e., including $K(q)$); in the weather regime, the spatial intermittency is even stronger: $K(2)/2 \approx 0.4$ (see *Lovejoy et al.* [2012] and LdL [Table 2], for global-scale weather regime estimates). Finally, we should note that, even when $K(2)/2$ is small, the probability distribution of the fluctuations may be far from Gaussian (Gaussian white noise would be flat, $K(2) = 0$). A clear example of non-Gaussian behavior in precipitation is given later, see Figure 7c.

These highly spatially averaged results raise the issue of the spatial homogeneity of the exponent: does H really vary from location to location or are the variation small enough to be essentially random estimation errors? In LdL, the time series were analyzed on a pixel by pixel basis and we found: $H \approx -0.41 \pm 0.07$, -0.38 ± 0.09, and -0.43 ± 0.10 for the GHCN, 20CR, and Smith data, respectively (the uncertainties are the

Table 4. Comparison of Macroweather Scaling Exponents for Different Precipitation Products (All at 1 Month, Anomalies), in Time and Space[a]

Scaling Exponents		GHCN	20CR	Smith	CPC
H	Time	-0.4	-0.4	-0.4	-0.42
	Space	-0.2	0.2	0.1	
C_1	Time	0.01	0.02	0.01	0.035
	Space	0.11	0.11	0.18	

[a] GHCN refers to the Global Historical Climate Network; "20CR," the Twentieth Century Reanalysis; "Smith" the *Smith et al.* [2012] IR satellite data-based product; and CPC, the Climate Prediction Center. The effective external spatial scales are between roughly 10,000 and 50,000 km (see LdL). The H, C_1 estimates for the spatial 20CR and Smith are the averages of the zonal (EW) and meridional (NS) values over the range $<50°-80°$. Note that over the range $>50°$–$80°$, both the Smith and 20CR spatial H values are ≈ -0.2 in agreement with the GHCN value. In space, the H values of the raw data are 0.2 for the 20CR and 0.15 for the Smith data (LdL). The outer scales of the 20CR and Smith were estimated using trace moments analysis to be approximately 25,000 km (for more details, see LdL). The CPC data (Figure 2a) are from *Lovejoy et al.* [2012].

standard deviations of the pixel to pixel variations; for regressions from each individual pixel, the uncertainty in the H values were nearly always in the range ± 0.02 to ± 0.03, so the pixel to pixel variations are statistically significant). The corresponding estimates of the intermittency parameter C_1 were: 0.026 ± 0.02, 0.020 ± 0.025, and 0.00 ± 0.01. H is thus roughly globally constant with a value ≈ -0.4. In order to see if the spread is simply due to estimation errors, in Figure 2b, we show the spatial distribution of H estimates. There is some spatial organization and reasonable agreement between the GHCN and 20CR maps, less agreement with the Smith map. There is also a tendency for H to be low over oceans (especially the Pacific); this is physically plausible since H values closer to zero correspond to longer range memory and hence predictability [*Lovejoy et al.*, 2015]. However, the values should be taken with caution since the 20CR temperatures have lower H over the oceans and the 20CR estimates of the precipitation are rather indirect.

A comparison of the macroweather scaling exponents is given in Table 4, for the different precipitation products (all at 1 month), in time and space, in particular for parameters H and C_1. The macroweather precipitation anomaly fluctuation exponents (H) were generally not estimated with high accuracy partly because of the high intermittency (the scaling was noisy) but also because more exact values are not warranted since the exact limits of the scaling ranges are not clear (because of this, the philosophy adopted in the relevant figures was to show reference lines rather that regression lines, for illustrating the estimates of H). This uncertainty in the limits of the scaling regime also limits the relevance of the standard statistical uncertainty estimates. Note that while the data agree very well on the temporal exponent, they disagree strongly on the spatial exponent including its sign (see section 5, below). For the spatial 20CR and Smith fields where the absolute precipitation rates were known, the spatial Hs for the raw and anomaly fields were quite close (see e.g., Figure 9d, discussed below). For the macroweather intermittency parameter C_1 in Table 4, note that the "time" column refers to pixel-scale spatial resolutions. The macroweather intermittencies (C_1) are significantly lower than the corresponding weather values, especially in time; the temporal C_1 of globally averaged values are slightly higher. The spatial macroweather C_1 parameters were estimated using trace moments in LdL.

4.2. Pixel and Global-Scale Temporal Precipitation Variability

We now use Haar structure functions (section 3.1.2) to explore the effect of spatial averaging on the temporal variability; we compare products of different spatial resolutions (pixel and global scale). Figures 3a and 3b show land, ocean, and global comparisons of GHCN, 20CR, and the Smith products. The interpretation of Figure 3a (see also Figure 3b) is thus straightforward: we see that out to at least 10–30 years, the scaling with exponent -0.4 is fairly well followed by all the data sets (there is a bit of a broad "bump" near $\Delta t = 1$ year especially in the Smith series indicating that the annual cycle has not been fully removed). Considering the top three curves in Figure 3a (land), we see that, at small Δt, the GHCN data are indeed more variable (by almost exactly a factor of 2), and this to at least 10–30 years. We also see that the Smith series is more variable than the 20CR series (at weather scales, the somewhat low 20CR variability has been quantified) [see *Lovejoy et al.*, 2012]. These RMS fluctuations' differences quantify the different visual appearances (e.g., the different degrees of smoothness) of the curves in Figure 1.

The fact that the curves in Figure 3a are roughly parallel—hence, that they differ by constant factors—may reflect differing "effective" spatial resolutions (i.e., their primary difference may be differing amounts of spatial averaging) since, for the GHCN data, fluctuations diminish rapidly in amplitude with the spatial resolution; this is because the spatial fluctuation exponent is negative: $H_x \approx -0.2$, see Table 4. Finally, note the break in the scaling at about 10 years in the 20CR curves which is particularly pronounced for

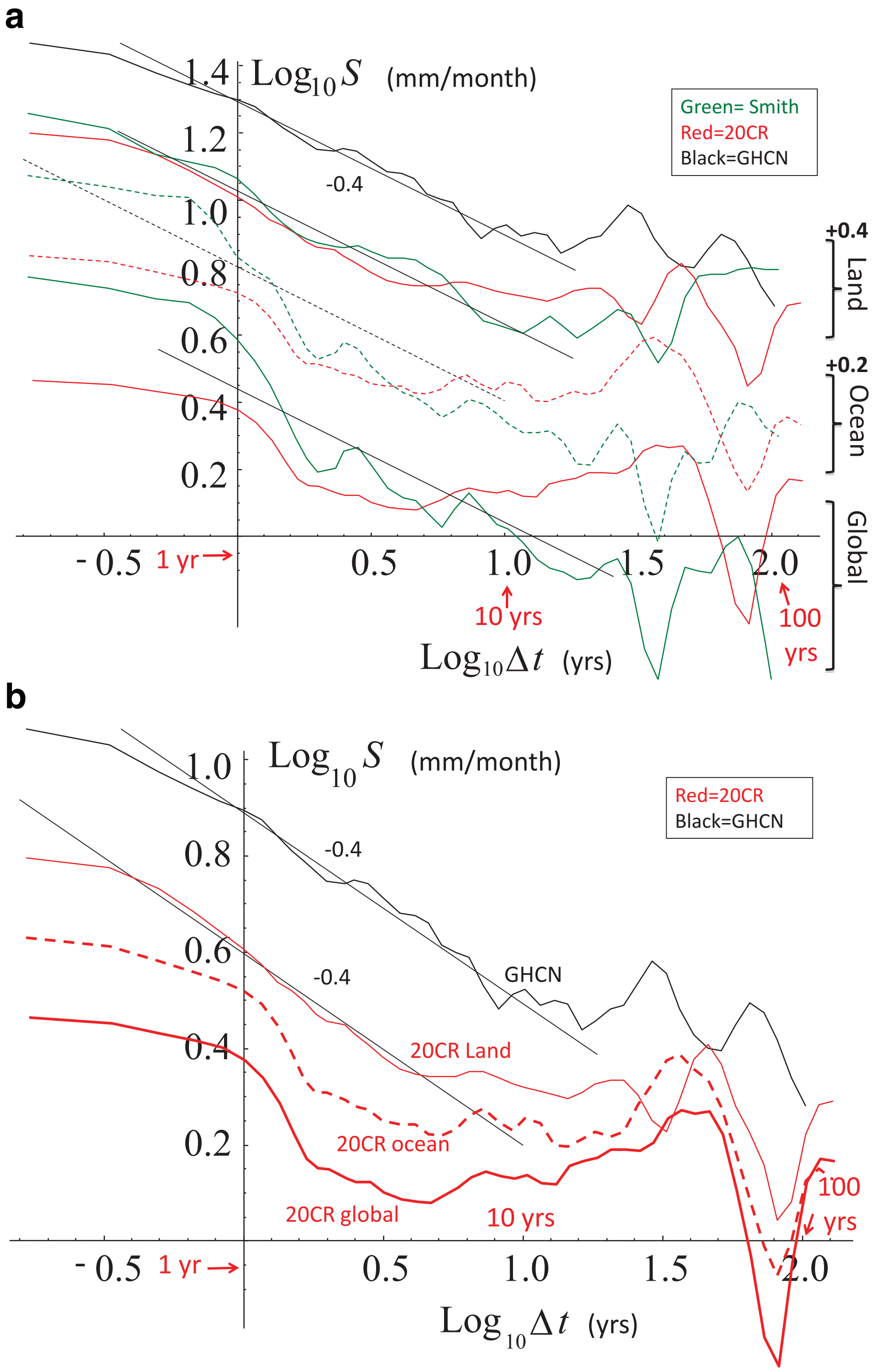

Figure 3. (a) Comparison of the Haar structure functions $S = \langle \Delta R(\Delta t)^2 \rangle^{1/2}$ for the land, ocean, and global GHCN (black), 20CR (red), and the Smith product (green; the global-scale series in Figure 1 were analyzed). The ocean and land curves are offset in the vertical for clarity by the amounts indicated (+0.2 and +0.4, respectively). The reference line has a slope of −0.4. (b) The same as Figure 3a, but with the global 20CR curve and the (land only) global GHCN curve. The global 20CR is lower than the land and ocean curves because it involves more spatially averaging. Notice that at 1 year scales, it is nearly a factor of 3 lower than the GHCN curve (the corresponding ratio for the moment $q = 1$ is 2.28). Reference lines with slopes −0.4 are shown. Note that the amplitudes decrease (top to bottom) as the area over which the averages are taken increases from the GHCN land only pixels to the 20CR global.

the ocean data; this is seen more clearly in Figure 3b. In a future publication, we argue that this break is a low-frequency anthropogenic effect. The fact that the break is much stronger over ocean than land helps to explain why anthropogenic effects on precipitation are so difficult to detect (e.g., the

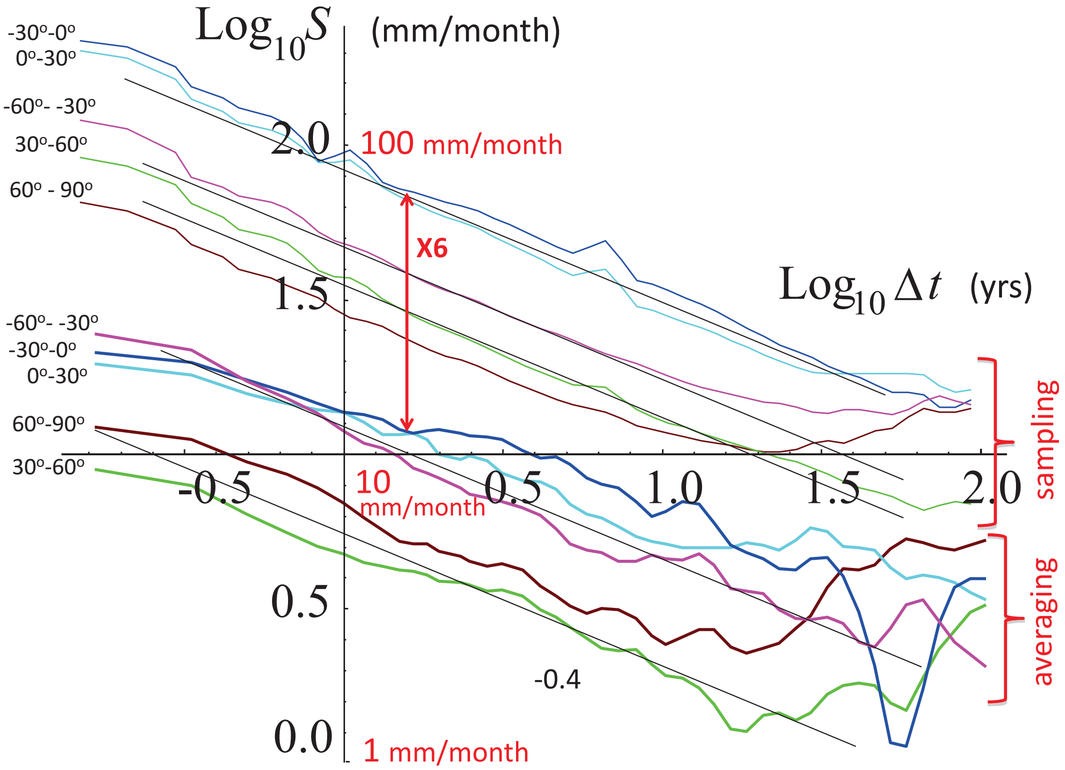

Figure 4. The Haar structure function for the GHCN data at pixel scales. The data were divided into 30° latitude bands (only five are shown since the southernmost, $-90°$ to $-60°$, band did not have enough data). The top set of curves (thin) are at 5° ("sampling"), the bottom set (thick) are spatially averaged over the band and then analyzed in time. The black reference lines have slopes $\xi(2)/2 \approx -0.4$.

International Panel on Climate Change (IPCC) Fourth and Fifth Assessment Reports—AR4 and AR5—respectively, *IPCC* [2007] and *IPCC* [2013]). In addition, the break/transition scale is a little larger than 10 years so that 10 year trend statistics have very low sensitivities to anthropogenic changes in precipitation; this helps explain why postulated multidecadal and centennial-scale anthropogenic increases in precipitation have not been identified with high levels of confidence.

To further understand the temporal variability, we can consider the RMS fluctuations $S(\Delta t)$) for different latitudes. Figure 4 shows the analysis of the GHCN data over five 30° latitude bands. The figure shows analyses at $5° \times 5°$ ("pixel" scale) resolution (top set) and $30° \times 360°$ resolution (i.e., spatially averaged over the whole band, the bottom set). The pixel-scale analyses had to contend with the large amount of missing data, thus a special Haar algorithm described in *Lovejoy* [2014b, Appendix A] was used. The pixel-scale analyses show nearly perfect scaling (again, with exponent $\xi(2)/2 \approx H = -0.4$) with the strongest break being in the band 60°–90°. By considering the spatially averaged curves, we can more easily notice the break and even discern a low frequency increasing $S(\Delta t)$ regime, in particular for the 60°–90° curve. Also note that the effect of spatial averaging is to reduce the fluctuations by roughly a factor 6 (as indicated by the red arrow); this is due to the negative spatial fluctuation exponent $H_x \approx -0.2$ (first-order moment, Table 4) and strong spatial intermittency (that amplifies this resolution effect for higher-order moments since $K(q) > 0$ for $q > 1$, see (5, 6)). Notice that the averaged curves deviate from the straight lines much more clearly than the 5° curves, presumably, since by averaging out the natural variability, the anthropogenic signal is (relatively) more important.

We can also consider the pixel-scale relationships between the different series both over 30° latitude bands (Figure 4) and with pixel-scale statistics averaged globally, see Figure 5. Also, in Figure 4, the scale break moves to shorter times as we move further north, which is consistent with an anthropogenic effects being stronger at northern latitudes. In Figure 5, we note that the Smith data show the best scaling at large Δt, the 20CR the worst (largest break).

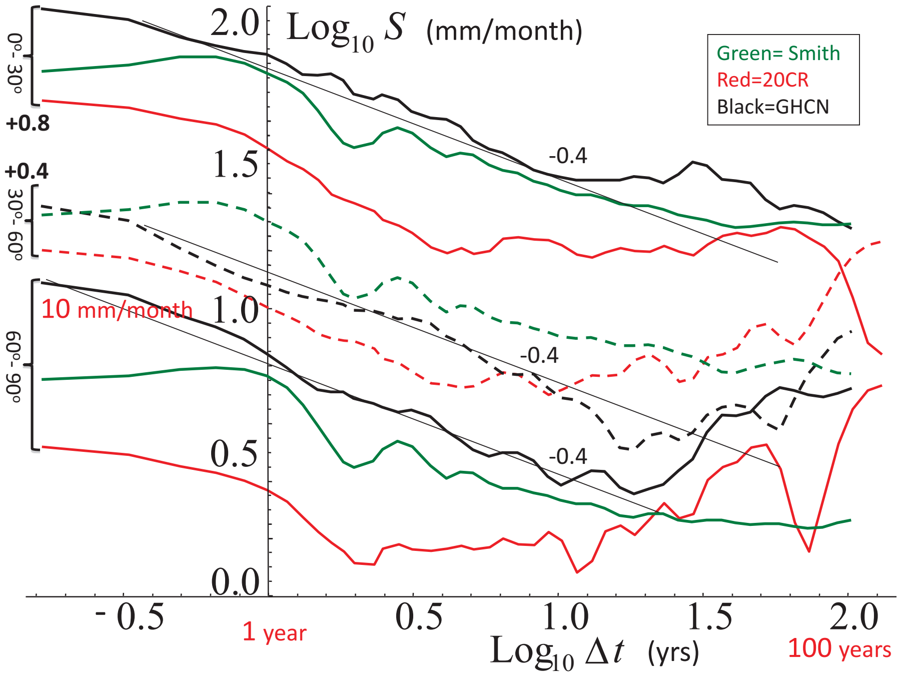

Figure 5. A comparison of the various data products over northern latitude bands (the Southern Hemisphere was roughly symmetrical and is not shown to economize on space), using the structure functions of Haar fluctuations. (top) The 0°–30° curves have been displaced upward by 0.8 for clarity (i.e., a factor $\approx$ 6.3); similarly, (middle) the 30°–60° curves (dashed) have been shifted upward by 0.4 (a factor $\approx$ 2.5). The 20CR data were degraded to 5° × 5° so that its resolution was the same as the two other series. The black curves are for the GHCN data, the green curves are for the Smith data, and the red curves are for the 20CR. The black reference lines have slopes $\xi(2)/2 \approx -0.4$.

It is also interesting to compare and contrast the RMS fluctuations of the GHCN product at its highest resolution 5° × 5°, averaged over all the pixels, with the RMS analysis of the (single) globally averaged series, see Figure 6. First, we note that the pixel and global-scale GHCN are virtually identical in shape, but differ by a factor of nearly 10. This is a pure resolution issue: the fact that the shape is the same is due to the spatial scaling (for the mean, $H_x \approx -0.2$, see Table 4), the fact that it is such a large factor is a symptom of the high-precipitation spatial intermittency (multifractality) that amplifies this effect for the higher-order moments (see section 5, below). The scaling exponent $\xi(2)/2 \approx H$ is again ≈ -0.4 with deviations starting to be noticeable at about 20 years. In comparison, the RMS global temperature fluctuations have a smaller slope ($\xi(2)/2 \approx H \approx -0.2$) and the transition (the scale break associated with anthropogenic effects) [*Lovejoy*, 2014a] starts at shorter time scales and is much stronger.

4.3. Temporal Variability of Individual Stations

The analysis of station data can help put the analysis of the global precipitation products in perspective, namely by comparing the temporal fluctuation statistics of the gridded GHCN product (obtained by combining series from several individual stations at each grid point), with those from individual stations; such analysis can provide insights into the importance of station data and also the spatially averaged gridded estimates. Thus, similarly to the precipitation products, the station data need to be explored using Haar fluctuation analysis (not only rain rates or anomalies, as it is usually done for single station data—see e.g., the relevant studies referenced in section 1). Figures 7a and 7b give some examples using instrumental data from near-complete exceptionally long monthly series from Portugal: 15 precipitation series (Figure 7a) and 9 temperature series (Figure 7b); see section 2 for the different origins of the series. In Figure 7a, in order to bring out the low-frequency break, we have compensated the structure function by multiplying by $\Delta t^{0.45}$, so that flat behavior indicates a power law decay with $\Delta t^{-0.45}$. The transition becomes noticeable in most (but not all) of the series after about 40 years. Once again, the comparison with temperature statistics (for a subgroup of the same stations, Figure 7b) shows that the break is more pronounced, it is at smaller Δt and the low-frequency variability is stronger.

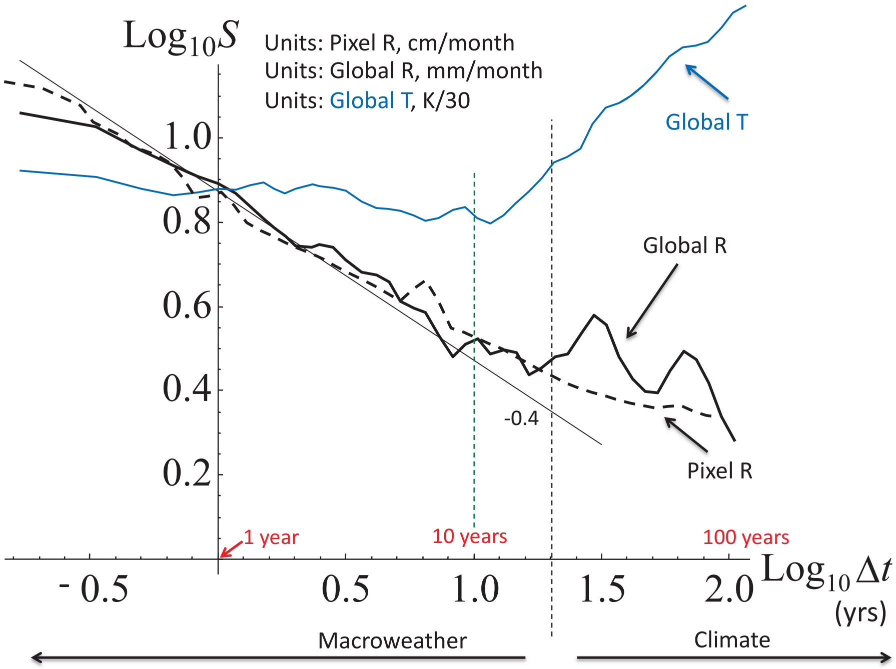

Figure 6. A comparison of global and pixel-scale GHCN RMS Haar fluctuations (all at monthly resolutions) with the corresponding analyses of the ensemble average of the three surface temperature series (HadCRUT3, NOAA CDC, and NASA GISS, original analysis and details in *Lovejoy and Schertzer* [2012a]). Note that the units for the global and pixel ($5^\circ \times 5^\circ$) GHCN data are different (mm/month and cm/month, respectively). The fact that they nearly overlap shows that the effect of spatial averaging is to reduce the amplitude of the variability by a factor of almost exactly 10. The units of the temperature fluctuation are in K if the values are reduced by a factor of 30. Notice that the macroweather/climate temperature transition time scale is roughly a factor of about 2 lower than for the precipitation transition scale (the pixel-scale temperature transition scale is closer to 20–30 years, see also Figure 7b and *Lovejoy et al.* [2013a]).

We have also explored the probability that a random monthly precipitation rate change/difference ΔR exceeds a fixed threshold s, for these 15 station series (pooled); the probability distribution $Pr(\Delta R > s)$ is shown in Figure 7c. The data illustrate that even if the second-order statistics are close to those expected for a Gaussian (i.e., $\xi(2)/2 \approx H$), that macroweather precipitation statistics may nonetheless be non-Gaussian: for ΔR exceeding a high enough fixed threshold s, we find $Pr(\Delta R > s) \approx s^{-q_D}$ with $q_D \approx 3.6$ (a bit lower than the macroweather temperature value $q_D \approx 5$, but close to the weather-scale precipitation value $q_D \approx 3$; see *Lovejoy and Schertzer* [2013, Chapter 5] for a review, which includes 12 references with similar q_D values). For example, for macroweather precipitation in Portugal, *de Lima* [1998] reports the values of $q_D \approx 3.5$ for gauge data from Vale Formoso (1932–1990, semiarid climate; mean annual precipitation: 566 mm) and $q_D \approx 5.7$ for Coimbra (1901–1990, maritime climate; mean annual precipitation: 990 mm).

4.4. How Reliable, How Accurate Are the Series at Different Time Scales?

We can now use the results discussed in section 3.1.4 to interpret the structure function plots and compare the precipitation products at different time scales. If the RMS fluctuations of the individual series $\langle \Delta R_1(\Delta t)^2 \rangle^{1/2}$, $\langle \Delta R_2(\Delta t)^2 \rangle^{1/2}$ are plotted on log-log plots, then for positively correlated series, the RMS difference fluctuations $\langle \Delta\delta R(\Delta t)^2 \rangle^{1/2}$ are bounded above the maximum of the two curves plus the constant $(\log_{10}2)/2 \approx 0.15$ (see (9)). This provides a convenient point of comparison when interpreting the figures (if the difference is larger—the maximum possible being $(\log_{10}2) \approx 0.30$—then the series are negatively correlated). For example, Figure 8a compares the GHCN and 20CR (anomaly) data at $5^\circ \times 5^\circ$ pixel scales, with double-headed arrows of length 0.15 (i.e., $\log_{10}(2^{0.5})$) shown for reference. We see that while the statistics of the two series (green and blue in the figure) are quite close over the entire available range of time scales, that they are not always very highly correlated with each other: at scales up to about 1 year they are nearly statistically independent with a similar comment for scales greater than about 20 years. We could mention

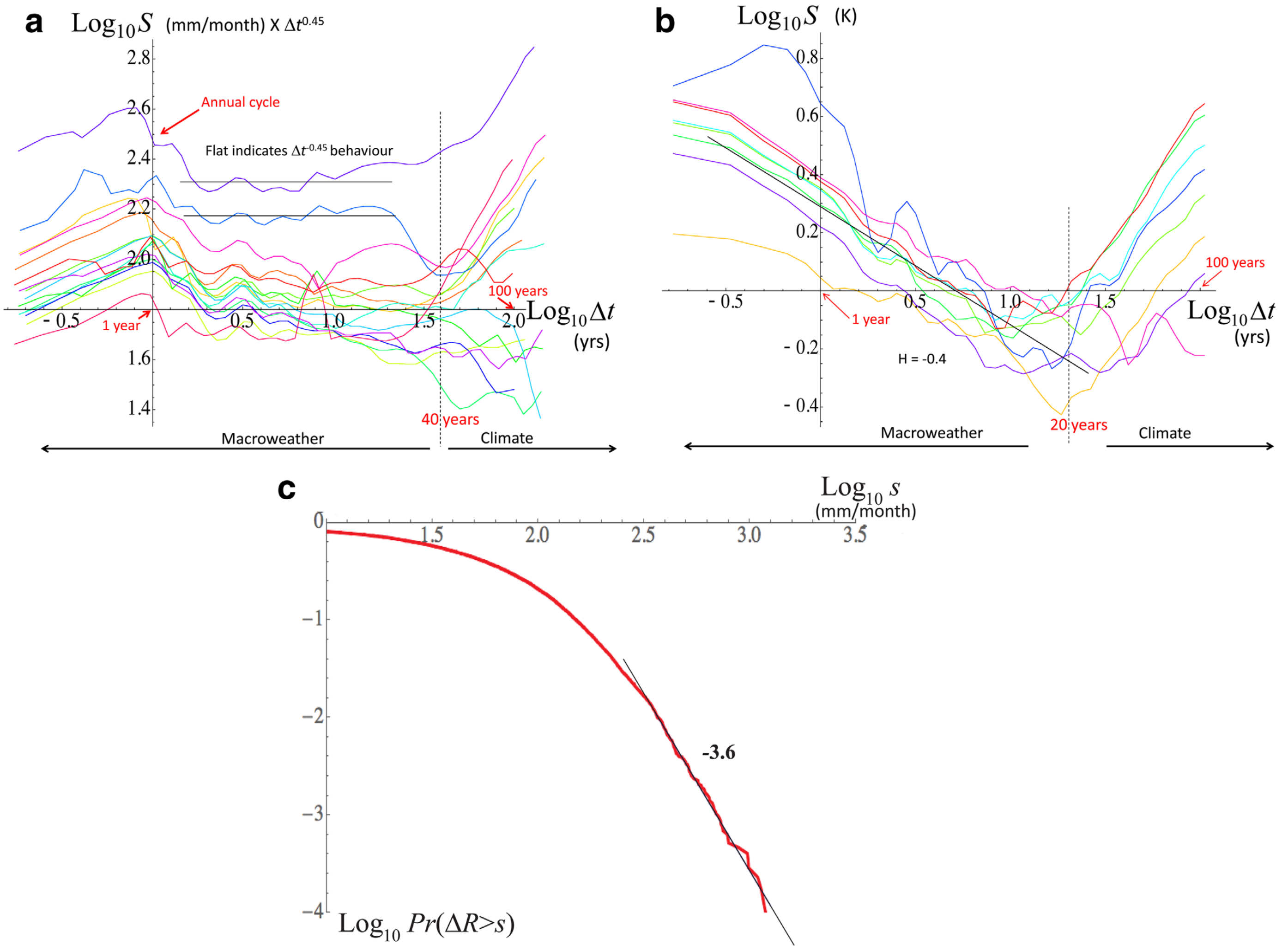

Figure 7. (a) The RMS Haar structure functions for monthly resolution precipitation from 15 individual Portuguese stations, chosen for their long lengths (data outages were not interpolated). In order to bring out the change in behavior at ≈40 years (where low-frequency climate processes, presumably primarily anthropogenic in origin, become dominant), we have "compensated" the structure functions by multiplying by $\Delta t^{0.45}$. Note that there is a "bump" at around 1 year due to the annual periodicity. This periodicity was not removed since the data had sufficiently numerous outages to make this difficult to do. Note that the overall behavior is quite similar from one station to another, although the overall amplitude (a vertical translation on this log-log plot) varies by about a factor 7. (b) The analysis for nine of the Portuguese stations in Figure 7a (eight series from mainland Portugal and one series from the Azores), but for monthly temperature fluctuations. The data cover periods between 114 and 148 years (the end date is 2010 for all series); the data selection was based on the length of the series and their degree of completeness. There is no interpolation for missing data and no compensation (RMS fluctuations in units of K). Notice that the transition from macroweather to climate is strong and occurs at ≈20 years rather than ≈40 years. (c) The probability distribution, $Pr(\Delta R>s)$: the probability that a random monthly precipitation rate change/difference ΔR exceeds a fixed threshold s; units: mm/month for the data (pooled) from the 15 Portuguese stations used in Figure 7a. The reference line shows the power law tail $Pr(\Delta R > s) \approx s^{-q_D}$ with absolute slope $q_D = 3.6$.

that our analysis is essentially equivalent to a cross-correlation analysis—but of the fluctuations, not of the series themselves: $\langle \Delta R_1(\Delta t)\Delta R_2(\Delta t)\rangle = \frac{1}{2}\left(\langle \delta\Delta R(\Delta t)^2\rangle - \langle \Delta R_1(\Delta t)^2\rangle - \langle \Delta R_2(\Delta t)^2\rangle\right)$.

Figure 8b shows the comparison of the two data sets that have no missing data: the 20CR and Smith series, categorized into land, ocean, and global (Figure 8a was for land only due to the limitations of the GHCN data). Notice that the RMS difference fluctuations (the difference between the Smith series and the 20CR, brown curve) are systematically larger than the maximum of the corresponding 20CR and Smith fluctuations indicating generally poor agreement; in Figure 8b, the arrows at around 5–10 years are placed at scales Δt where the two curves are nearly equal so that it can be seen that the difference is about the same as for independent processes. At scales larger than about 10 years (especially for the global curve), the differences become somewhat smaller, indicating an increasing measure of agreement. The low-frequency divergence between the products is because they disagree in the break in the scaling, itself expectedly associated with different estimates of anthropogenic effects.

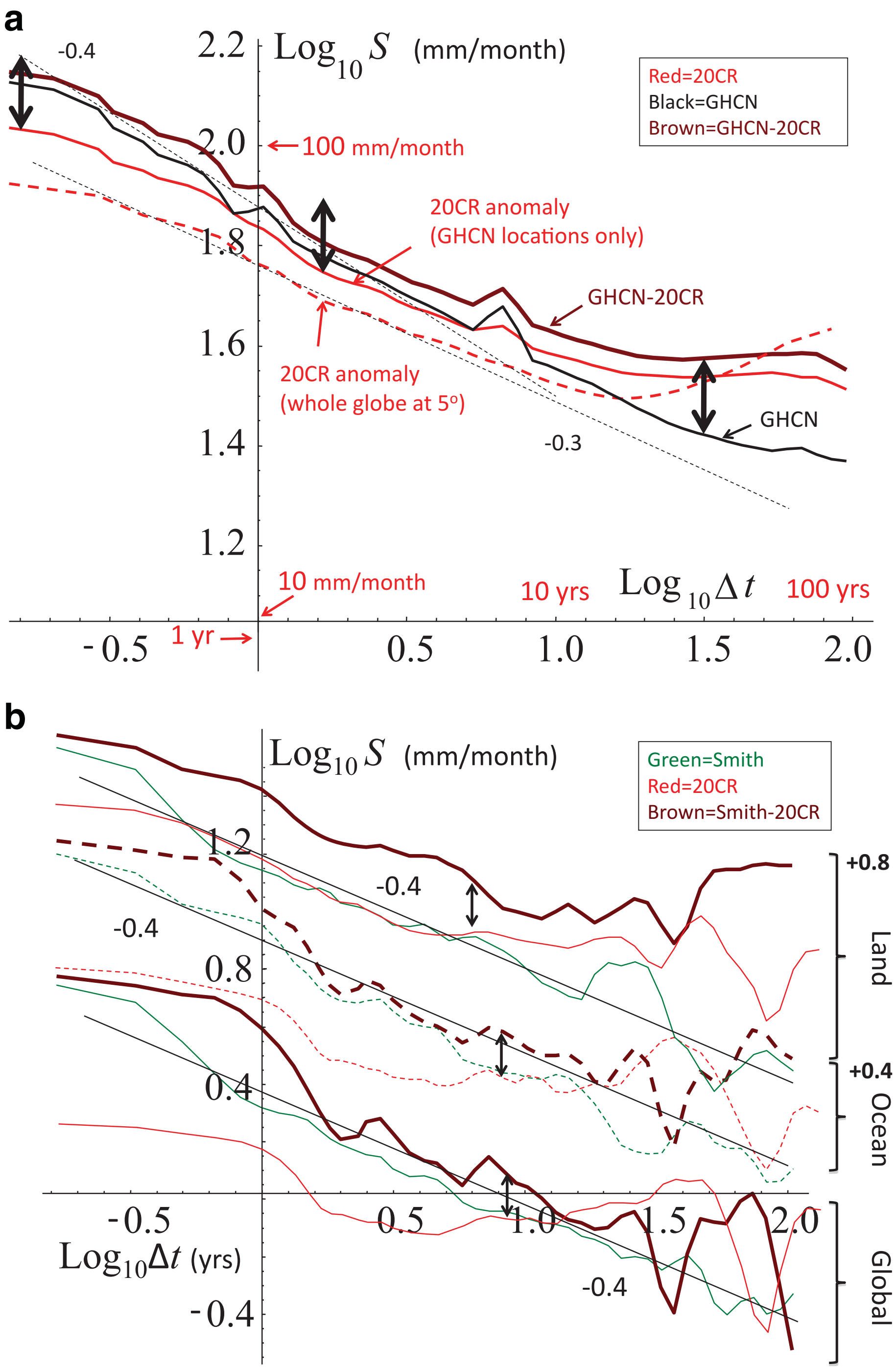

Figure 8. (a) The temporal RMS Haar structure functions for the GHCN and 20CR precipitation products at 5° × 5° pixel scale. The original (1.875° × 1.875°) 20CR data were first converted into anomalies by subtracting the long-term mean of the annually detrended data. The monthly 20CR product was degraded to the same 5° × 5° grid at the GHCN product. The pixel-scale GHCN curve from Figure 6 is shown (black) along with the 20CR curves ensemble averaged over all the (5° × 5°) pixels (*whole globe*; red, dashed) and only over the same pixels as the GHCN data (*land*; red, solid). Also shown is the corresponding structure function of the differences in the GHCN and 20CR anomalies (brown, thick upper curve). Notice that the differences are about the same as the values (two uncorrelated series would have differences with double the variance, hence a factor $2^{0.5} \approx 1.4$ difference; the double-headed arrows indicate the factor $2^{0.5}$). Reference lines with slopes -0.3 and -0.4 (20CR and GHCN, respectively) are given. (b) Comparison of the temporal RMS Haar structure functions for the global-scale Smith series (green) and differences (brown, thick) with the 20CR series (red). The land curves (upper curves) were displaced upward by 0.8 for clarity, the ocean curves (middle, dashed curves) by 0.4. The double-headed arrows indicate the factor $2^{0.5}$, which would be the upward shift of RMS fluctuation of the differences of two statistically identical but statistically independent products.

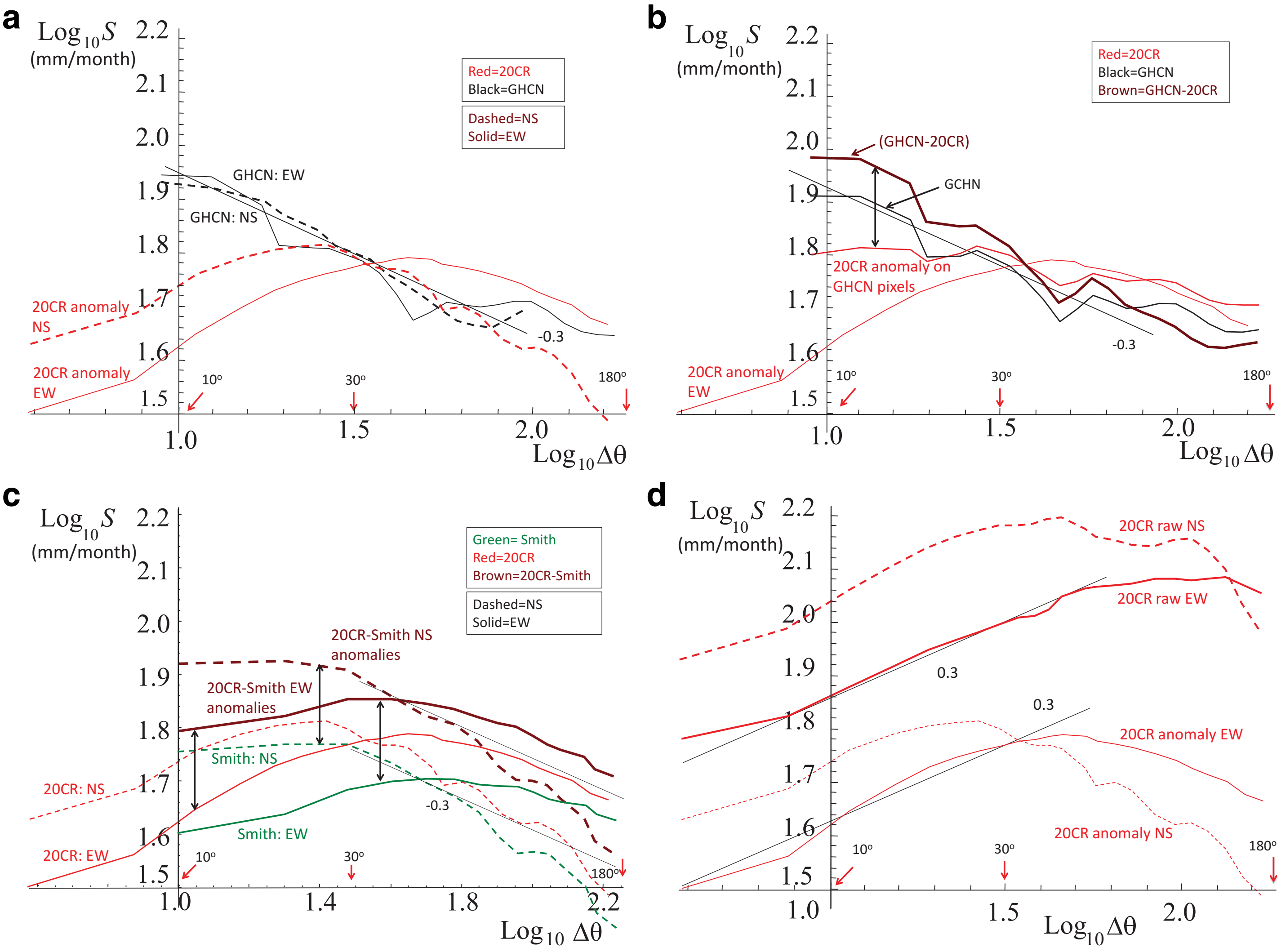

Figure 9. (a) A comparison of the GHCN (anomalies, 5° × 5°, land, black curves) with the 20CR anomalies (at 1.875° × 1.875°, land only, red curves), monthly data, $\Delta\theta$ is the angular scale in degrees. RMS Haar spatial structure functions are shown in the EW (solid) and NS (dashed) directions. Notice that there is close agreement for distances greater than about 20°. The reference line has slope $\xi_x(2)/2 \approx -0.3$. (b) Monthly east-west Haar structure functions for 20CR anomalies (at 1.875°, the whole earth; long thin red curve) and the others at 5° resolution, only over the same pixels as the GHCN data (red, short curve). Also shown is the GHCN east-west structure function (black) along with the structure function of the difference between the GHCN and the 20CR anomalies (brown, thick curve). The GHCN and 20CR structure functions agree quite well past 20° yet the difference between them is still quite large. The double-headed arrows show the length 0.15, corresponding to statistical independence of identical processes, see (9) showing that at about 10°, the GHCN, 20CR products are nearly statistically independent. $\Delta\theta$ is the angular scale in degrees. The reference line has slope $\xi_x(2)/2 \approx -0.3$. (c) A comparison of the RMS spatial fluctuation statistics of the 20CR (red) anomalies along with the Smith anomalies (green) and RMS fluctuations of the differences (thick, brown); $\Delta\theta$ is the angular scale in degrees. The functions are shown in the EW (solid) and NS (dashed) directions. The reference line has slope $\xi_x(2)/2 \approx -0.3$. The double-headed arrows show the length 0.15 corresponding to statistical independence of identical processes, see (9). (d) A comparison of the RMS Haar 20CR structure functions for anomalies (thin, bottom) and raw precipitation rates (thick, top) in both the EW (solid) and NS (dashed) directions. $\Delta\theta$ is the angular scale in degrees. Reference lines with slopes $\xi_x(2)/2 \approx 0.3$ have been added.

Overall, for data at 5° × 5° spatial resolution, the GHCN and 20CR are thus closest with reasonable agreement at annual and larger scales whereas even at global spatial scales, the Smith data are in poor agreement with the 20CR until decadal scales.

5. Spatial Macroweather Precipitation Statistics

In this section, we explore the spatial fluctuation statistics in macroweather precipitation using the approach described in section 3.2. Both raw data and anomalies are inspected, and the statistics are compared for the two data types.

We now turn to the RMS Haar structure functions in Figure 9a that compares the spatial anomalies for the GHCN, 20CR data in both the zonal (EW) and meridional (NS) direction. We see that the GHCN anomalies are reasonably scaling with RMS exponent $\xi_x(2)/2 \approx -0.3$ and that for scales larger than about 30° ($\approx$3000 km at the equator), the 20CR has very similar statistics (for the spatial statistics, we do not use the approximation $\xi_x(2)/2 \approx H_x$, see below). Notice however that even at scales as large as 10°, they differ by roughly a factor of 2 in their RMS amplitudes.

More insight is obtained by considering their differences δR in Figure 9b. This confirms that at scales below about 30°, the spatial distributions are nearly statistically independent with agreement becoming significant only at distances of 30° and more. It seems likely that the 20CR anomalies at scales below about 30° are artificially smoothed resulting in positive slopes rather than negative (high variability) slopes of the instrumental GHCN anomalies. For the spatial comparisons at 1 month temporal resolution, we see that the 20CR and GHCN are reasonably in agreement at scales of 20°–30° of arc and larger whereas the Smith data are in poor agreement with the 20CR until at least 50° of arc.

We can also compare the 20CR and Smith data (Figure 9c). Again, we see nearly a factor of 2 difference in variabilities at smaller scales (at 10°, the Smith data are smoother), with very low spatial correlations (nearly statistical independence at the left hand side of the graph), but with some limited convergence at the largest scales. For the Smith data there is no clear spatial scaling regime. Note that the Smith data are based on satellite measurements after 1979 and gauge data before this date. However, the spatial H for the Smith data is very close to that of the satellite IR data that were used to estimate it [*Lovejoy et al*., 2009]; we therefore do not expect a big change in behavior before and after 1979.

Finally, we can compare the analysis of the anomalies and raw RMS fluctuations. For the 20CR product, Figure 9d shows that they follow each other fairly well up to $\approx$30°, with the RMS anomaly fluctuations about a factor of 2 smaller. Also of note is the scaling of the raw rain rates which have positive slopes ($\xi_x(2)/2 \approx 0.3$) and which continue up to quite large scales (especially in the zonal direction where it continues up to $\approx$90°, i.e., 10,000 km; the 20CR and Smith anomalies for $\Delta\theta \approx <30°$ are probably not trustworthy, see Figures 9a–9c). By comparing the raw fluctuations in Figure 9d with those of the anomalies in Figures 9a and 9b, it is plausible that the spatial scaling of the raw data has a quite different exponent ($\xi_x(2)/2 \approx 0.3$) from the anomalies ($\xi_x(2)/2 \approx -0.3$).

The overall conclusion of the comparisons of the three data sets using the fluctuations of the differences is that in time, at 5° × 5° resolution, the GHCN and 20CR are quite close at a scale of about 1 year and longer whereas even the globally averaged 20CR and Smith data are dissimilar until decadal scales and are different at the longest scales. At 1 month resolution, the GHCN and 20CR were similar at scales larger than 20°–30° of arc whereas the 20CR and Smith were quite dissimilar until at least 50° of arc. The obvious interpretation is that the GHCN and 20CR are the most reliable (because the most similar).

Although it is outside of the scope of this work to characterize the space-time variability in precipitation, its importance deserves a brief discussion. A full characterization of the space-time variability involves determining the joint space-time fluctuation statistics, for example, the structure functions of fluctuations $S(\Delta x, \Delta t) = \langle \Delta R(\Delta x, \Delta t)^2 \rangle^{1/2}$. It turns out that if space-time turbulent cascade models (that model the weather regimes) are extended to the macroweather regime by the simple expedient of greatly increasing the temporal outer scale, it leads to a model (EFIF) that approximately satisfies a space-time statistical factorization property [*Lovejoy and Schertzer*, 2010, 2013]. For example, it predicts the approximate relation:

$$S(\Delta x, \Delta t) \approx S_x(\Delta x) S_t(\Delta t) \tag{14}$$

where $S_x(\Delta x)$ and $S_t(\Delta t)$ are the spatial and temporal structure functions determined above. The physical interpretation is that $S_x(\Delta x)$ represents the statistical variation from one climatic zone to another and the climatic zones spatially modulate the temporal statistics which are otherwise of the same basic form. This is discussed and tested and generally well confirmed in LdL.

6. Discussion and Conclusions

While several studies have considered single station (i.e., temporal) precipitation statistics from weeks to decades (and occasionally century) scales—the macroweather regime—a clear picture of temporal macroweather statistics has not emerged. In addition, there have been virtually no studies of spatial macroweather precipitation, i.e., of the spatial variability of precipitation fields averaged over weekly, monthly, or longer periods yet their characterization is needed to construct macroweather models. In this paper, we explored three relevant global-scale macroweather precipitation products: the Global Historic Climate Network product (GHCN) [*Vose et al*., 1992], which are the conventional station precipitation series restricted to land only; in addition, the globally complete Twentieth Century Reanalysis product (20CR) [*Compo et al*., 2011] and the satellite-based product [*Smith et al*., 2012]. Thus, by analyzing these precipitation products (land, ocean, and global) and adopting a scaling framework, we expected (a) to clarify the character of weather and macroweather precipitation regimes, (b) to better understand the limitations of different precipitation products, and (c) to explain the space-time macroweather precipitation variability, relevant for the stochastic modeling and forecasting of macroweather fields. Also, by analyzing monthly, centennial, instrumental station data, and comparing them with the relevant precipitation products, we aim at a better insight into some difficulties that often hamper assessing clearly the macroweather regime statistics from single station data analysis.

The statistics of precipitation as functions of space and time scale were studied using Haar fluctuations and statistically characterized using generalized structure functions. In spite of their simplicity, the Haar fluctuations allow precipitation to be analyzed over its full range of space-time scales (i.e., both $0<H<1$ and $-1<H<0$ regimes). We then systematically analyzed and compared the three products over the ranges from 1 month to $\approx$100 years and from one pixel (primarily $5^\circ \times 5^\circ$) to global scales. Results showed that even with Haar fluctuations, due to the extreme variability (high multifractal intermittency), that precipitation statistics have nonclassical behaviors. In the time domain, for all products, we found very similar behaviors: for land, ocean, global, and for various latitude bands for pixel and global scales, we found $H_t \approx -0.4$ which is a little higher than Gaussian white noise ($H=-0.5$); the main differences between the data sets are the amplitudes of the fluctuations (e.g., the RMS variability at a given scale such as 1 year) and the outer scale τ_c, the transition scale to the climate regime (here presumably associated with anthropogenic effects). The global-scale analyses had $\tau_c \approx 20$ years whereas the pixel-scale analyses (including several individual long station series from Portugal) had $\tau_c \approx 40$ years (presumably due to the smaller amount of averaging). Although the systematic analysis of anthropogenic effects was outside our scope, we noted that the breaks in the scaling of the global ocean precipitation rates were at somewhat shorter time scales than for the corresponding global land series as expected if the anthropogenic effects were stronger over the ocean.

These robust temporal scaling statistics may lead one to conclude that macroweather precipitation is well estimated, and this in spite of the quite different techniques used to estimate precipitation rates (instruments, reanalyses, and satellite based). However, the agreement of the statistics over wide ranges of time scales is only a necessary condition for the products to agree with each other, it is not sufficient: indeed, each product could be from a statistically independent realization of the same stochastic process. To gain further confidence in the quality, accuracy of the precipitation products, we therefore compared the product fields directly to each other by considering the difference of two products and studied the fluctuation statistics of the difference fields.

This analysis showed (section 4.4, time; section 5, space) that the agreement between the products was not so good. For example, for the GHCN and 20CR products at $5^\circ \times 5^\circ$ spatial resolution, the agreement at scales both below a year and also greater than 10 years was poor (Figure 8a). The 20CR and Smith products (the two that were not missing data) for times below about 5 years were in poor agreement with each other even at global spatial scales, and again displayed poor agreement at scales beyond about 30 years (Figure 8b). In space at 1 month resolution, the situation was somewhat different with agreement between the 20CR and GHCN for scales above 20°–30° arc and with the 20CR and Smith data only becoming at all close to each other at 50° of arc and larger (Figures 9b and 9c). It also seemed that the spatial scaling exponents were significantly different (see Table 4) with the 20CR and Smith products being much smoother (H_x about 0.4–0.5 larger—hence smoother—than for the GHCN product); the smoothness may be an artifact of the limitations of the 20CR model and the smoothness (larger H exponent) of the satellite IR fields that were used to infer the Smith product. Additionally, we have compared the precipitation statistics obtained for the raw data fluctuations with those of the anomalies, and concluded that the spatial scaling exponents can be quite different, although they agree over certain ranges of scale.

The macroweather spatial and temporal scaling properties of precipitation that we have identified are qualitatively very similar to those of macroweather temperatures as analyzed, for example, in *Lovejoy and Schertzer* [2012a, 2013]. The main differences between temperature and precipitation statistics is that the latter have generally lower temporal H values, higher spatial C_1 values (parameter C_1 characterizes the intermittency near the mean) and somewhat longer transition scales τ_c. Similar comments also pertain when comparing weather-scale temperatures and precipitation (although here, the intermittency parameter C_1 is much larger for precipitation than for temperature). Note that, regarding intermittency, there is an important (near) exception: the temporal macroweather precipitation variability, which has a small C_1 and is therefore not too far from being quasi-Gaussian, see Table 4; however, the extremes are very non-Gaussian (Figure 7c). Overall, both at weather and macroweather scales, of all the standard atmospheric fields, precipitation has the largest C_1. This higher intermittency explains why conventional analysis methods do not easily give evidence of anthropogenic changes in precipitation, as a consequence of warming, one must consider scales of several (3–4) decades for the anthropogenic "signal" to exceed the natural variability "noise." Similarly, it can explain the failure of clear trend to emerge at the local scale, from analysis of single station series, particularly if the data cover only a few decades, as it is often the case. Additionally, it is expected that anthropogenic effects may be primarily visible over the oceans since this is where increased heating is expected to translate most strongly into increased evaporation and precipitation, whereas many precipitation studies are limited to land only.

Our results indicate that precipitation may be treated in the same theoretical framework as the temperature (and other atmospheric fields): that it can be modeled with the help of space-time cascade processes. In this picture, the scaling laws are emergent high level statistical (turbulent) laws expected to apply in the limit of high nonlinearity. The weather/macroweather transition-scale τ_w is determined by the solar flux-induced energy rate density and the macroweather regime is a consequence of a "dimensional transition" in which the spatial degrees of freedom important for weather-scale processes become gradually "quenched" at time scales $\gg \tau_w$. A consequence (worked out in detail in *Lovejoy and Schertzer* [2013, Appendix 10A]) is that one generically obtains temporal macroweather exponents H in the range $-0.5 < H_t < 0$ (especially in the range $-0.4 < H_t < -0.2$). The model predicts that a statistical space-time macroweather factorization property should approximately hold—this means that, for example, the joint structure functions should also factor. *Lovejoy and de Lima* [2015] verify this on these same data sets, and propose a more direct space-time macroweather model, the ScaLIng Macroweather Model (SLIMM) that is multifractal in space (to account for the strong intermittency associated with different climate zones), yet monofractal (Gaussian) in time (since $C_1 \approx 0$ in time). Physically, the interpretation is that spatial variations in macroweather statistics are controlled by different "climatic zones" which modulate the otherwise qualitatively similar (scaling) temporal variability. In the time domain, SLIMM is a fractional Gaussian noise whose predictability properties are known, hence this provides the basis for seasonal, annual, and interannual (i.e., macroweather) precipitation forecasts.

The clarification of space-time macroweather precipitation variability, which was our concern in this work, is a necessary step for understanding macroweather precipitation and the limitations of the corresponding precipitation products, and opens new perspective to the stochastic modeling and forecasting of macroweather fields.

Acknowledgments
All data regarding the global precipitation products used in this work are properly cited and listed in the references. We thank A. Bussy for help with the analysis of the Smith product. The precipitation and temperature station data from Portugal were provided by F. Espírito Santo, Director of the Division of Climate and Climate Change of the Portuguese Sea and Atmosphere Institute (IPMA; http://www.ipma.pt/pt/index.html), for research purposes only; the data are available from IPMA, subject to IPMA's data policy. This work was unfunded, and there are no conflicts of interests.

References

Adler, R. F., et al. (2003), The version-2 Global Precipitation Climatology Project (GPCP) monthly precipitation analysis (1979–Present), *J. Hydrometeorol.*, *4*, 1147–1167, doi:10.1175/1525-7541(2003)004<1147:TVGPCP>2.0.CO;2.

Becker, A., P. Finger, A. Meyer-Christoffer, B. Rudolf, K. Schamm, U. Schneider, and M. Ziese (2013), A description of the global land-surface precipitation data products of the Global Precipitation Climatology Centre with sample applications including centennial (trend) analysis from 1901–present, *Earth Syst. Sci. Data*, *5*, 71–99, doi:10.5194/essd-5-71-2013.

Bunde, A., J. F. Eichner, J. W. Kantelhardt, and S. Havlin (2005), Long-term memory: A natural mechanism for the clustering of extreme events and anomalous residual times in climate records, *Phys. Rev. Lett.*, *94*, 048701, doi:10.1103/PhysRevLett.94.048701.

Bunde, A., U. Büntgen, J. Ludescher, J. Luterbacher, and H. von Storch (2013), Is there memory in precipitation?, *Nat. Clim. Change*, *3*, 174–175, doi:10.1038/nclimate1830.

Compo, G. P., et al. (2011), The Twentieth Century Reanalysis Project, *Q. J. R. Meteorol. Soc.*, *137*, 1–28, doi:10.1002/qj.776.

de Lima, M. I. P. (1998), Multifractals and the temporal structure of rainfall, PhD thesis, 225 pp., Wageningen Agric. Univ., Wageningen, Netherlands.

de Lima, M. I. P., and J. L. M. P. de Lima (2009), Investigating the multifractality of point precipitation in the Madeira archipelago, *Nonlinear Processes Geophys.*, *16*, 299–311, doi:10.5194/npg-16-299-2009.

de Montera, L., L. Barthès, C. Mallet, and P. Golé (2009), The effect of rain–no rain intermittency on the estimation of the Universal Multifractals Model parameters, *J. Hydrometeorol.*, *10*(2), 493–506, doi:10.1175/2008JHM1040.1.

Doswell, C. A., III, and S. Lasher-Trapp (1997), On measuring the degree of irregularity in an observing network, *J. Atmos. Oceanic Technol.*, *14*, 120–132.

Garcia-Marin, A. P., F. J. Jimenez-Hornero, and J. L. Ayuso-Munoz (2008), Universal multifractal description of an hourly rainfall time series from a location in southern Spain, *Atmosfera*, *21*, 347–355.

Giordano, F., I. Ortosecco, and L. Tramontana (1995), Fractal structure of marine measuring networks, *Il Nuovo Cimento C*, *18*(2), 177–182, doi:10.1007/BF02512018.

Gires, A., I. Tchiguirinskaia, D. Schertzer, and S. Lovejoy (2013), Development and analysis of a simple model to represent the zero rainfall in a universal multifractal framework, *Nonlinear Processes Geophys.*, *20*, 343–356, doi:10.5194/npg-20-343-2013.

Hoang, C. T., I. Tchiguirinskaia, D. Schertzer, P. Arnaud, J. Lavabre, and S. Lovejoy (2012), Assessing the high frequency quality of long rainfall series, *J. Hydrol.*, *438-439*, 39–51, doi:10.1016/j.jhydrol.2012.01.044.

IPCC (2007), *Climate Change 2007: The Physical Science Basis. Contribution of Working Group I to the Fourth Assessment Report of the Intergovernmental Panel on Climate Change*, 996 pp., Cambridge Univ. Press, Cambridge, U. K.

IPCC (2013), *Climate Change 2013: The Physical Science Basis. Contribution of Working Group I to the Fifth Assessment Report of the Intergovernmental Panel on Climate Change*, Cambridge Univ. Press, Cambridge, U. K.

Kantelhardt, J. W., E. Koscielny-Bunde, D. Rybski, P. Braun, A. Bunde, and S. Havlin (2006), Long-term persistence and multifractality of precipitation and river runoff record, *J. Geophys. Res.*, *111*, D01106, doi:10.1029/2005JD005881.

Kolesnikov, V. N., and A. S. Monin (1965), Spectra of meteorological field fluctuations, Izvestiya, *Atmos. Oceanic Phys.*, *1*, 653–669.

Korvin, G., D. M. Boyd, and R. O'Dowd (1990), Fractal characterization of the South Australian gravity station network, *Geophys. J. Int.*, *100*(3), 535–539, doi:10.1111/j.1365-246X.1990.tb00705.x.

Ladoy, P., S. Lovejoy, and D. Schertzer (1991), Extreme variability of climatological data: Scaling and intermittency, in *Non-Linear Variability in Geophysics: Scaling and Fractals*, edited by D. Schertzer and S. Lovejoy, pp. 241–250, Kluwer, Amsterdam, Netherlands.

Lovejoy, S. (2013), What is climate?, *Eos Trans. AGU*, *94*(1), 1–2.

Lovejoy, S. (2014a), Scaling fluctuation analysis and statistical hypothesis testing of anthropogenic warming, *Clim. Dyn.*, *42*(9), 2339–2351, doi:10.1007/s00382-014-2128-2.

Lovejoy, S. (2014b), A voyage through scales, a missing quadrillion and why the climate is *not* what you expect, *Clim. Dyn.*, *44*(11), 3187–3210, doi:10.1007/s00382-014-2324-0.

Lovejoy, S., and M. I. P. de Lima (2015), The joint space-time statistics of macroweather precipitation, space-time statistical factorization and macroweather models. *Chaos*, *25*(7), 075410, doi:10.1063/1.4927223.

Lovejoy, S., and D. Schertzer (1986), Scale invariance in climatological temperatures and the local spectral plateau, *Ann. Geophys.*, *4B*, 401–410.

Lovejoy, S., and D. Schertzer (2010), Towards a new synthesis for atmospheric dynamics: Space-time cascades, *Atmos. Res.*, *96*, 1–52, doi:10.1016/j.atmosres.2010.01.004.

Lovejoy, S., and D. Schertzer (2012a), Low frequency weather and the emergence of the climate, in *Extreme Events and Natural Hazards: The Complexity Perspective, Geophys. Monogr. Ser.*, edited by A. S. Sharma et al., pp. 231–254, AGU, Washington, D. C.

Lovejoy, S., and D. Schertzer (2012b), Haar wavelets, fluctuations and structure functions: Convenient choices for geophysics, *Nonlinear Processes Geophys.*, *19*, 1–14, doi:10.5194/npg-19-1-2012.

Lovejoy, S., and D. Schertzer (2013), *The Weather and Climate: Emergent Laws and Multifractal Cascades*, 496 pp., Cambridge Univ. Press, Cambridge, U. K.

Lovejoy, S., D. Schertzer, and P. Ladoy (1986), Fractal characterisation of inhomogeneous measuring networks, *Nature*, *319*, 43–44.

Lovejoy, S., D. Schertzer, and V. Allaire (2008), The remarkable wide range scaling of TRMM precipitation, *Atmos. Res.*, *90*, 10–32, doi:10.1016/j.atmosres.2008.02.016.

Lovejoy, S., D. Schertzer, V. Allaire, T. Bourgeois, S. King, J. Pinel, and J. Stolle (2009), Atmospheric complexity or scale by scale simplicity?, *Geophys. Res. Lett.*, *36*, L01801, doi:10.1029/2008GL035863.

Lovejoy, S., J. Pinel, and D. Schertzer (2012), The global space-time cascade structure of precipitation: Satellites, gridded gauges and reanalyses, *Adv. Water Resour.*, *45*, 37–50, doi:10.1016/j.advwatres.2012.03.024.

Lovejoy, S., D. Schertzer, and D. Varon (2013a), Do GCM's predict the climate. . .. or macroweather?, *Earth Syst. Dyn.*, *4*, 439–454, doi:10.5194/esd-4-439-2013.

Lovejoy, S., D. Schertzer, and I. Tchiguirinskaia (2013b), Further (monofractal) limitations of climactograms, *Hydrol. Earth Syst. Sci. Discuss.*, *10*, C3086–C3090.

Lovejoy, S., J. P. Muller, and J. P. Boisvert (2014), On Mars too, expect macroweather, *Geophys. Res. Lett.*, *41*, 7694–7700, doi:10.1002/2014GL061861.

Lovejoy, S., L. del Rio Amador, and R. Hébert (2015), The ScaLIng Macroweather Model (SLIMM): Using scaling to forecast global scale macroweather from months to decades, *Earth Syst. Dyn.*, *6*, 637–658, doi:10.5194/esd-6-637-2015.

Mazzarella, A., and G. Tranfaglia (2000), Fractal characterisation of geophysical measuring networks and its implication for an optimal location of additional stations: An application to a rain-gauge network, *Theor. Appl. Climatol.*, *65*, 157–163, doi:10.1007/s007040070040.

Nicolis, C. (1993), Optimizing the global observational network—A dynamical-approach, *J. Appl. Meteorol.*, *32*, 1751–1759, doi:10.1175/1520-0450(1993)032<1751:OTGONA>2.0.CO;2.

Olsson, J., and J. Niemczynowicz (1996), Multifractal analysis of daily spatial rainfall distributions, *J. Hydrol.*, *187*(1–2), 29–43, doi:10.1016/S0022-1694(96)03085-5.

Panofsky, H. A. (1969), The spectrum of temperature, *Radio Sci.*, *4*, 1143–1146, doi:10.1029/RS004i012p01143.

Pathirana, A., S. Herath, and T. Yamada (2003), Estimating rainfall distributions at high temporal resolutions using a multifractal model, *Hydrol. Earth Syst. Sci.*, *7*(5), 668–679.

Rysman, J.-F., S. Verrier, Y. Lemaître, and E. Moreau (2013), Space-time variability of the rainfall over the western Mediterranean region: A statistical analysis, *J. Geophys. Res. Atmos.*, *118*, 8448–8459, doi:10.1002/jgrd.50656.

Schertzer, D., and S. Lovejoy (1987), Physical modeling and analysis of rain and clouds by anisotropic scaling of multiplicative processes, *J. Geophys. Res.*, *92*, 9693–9714.

Smith, T. M., P. A. Arkin, L. Ren, and S. S. P. Shen (2012), Improved reconstruction of global precipitation since 1900, *J. Atmos. Oceanic Technol.*, *29*, 1505–1517, doi:10.1175/JTECH-D-12-00001.1.

Sun, X., and A. P. Barros (2010), An evaluation of the statistics of rainfall extremes in rain gauge observations, and satellite-based and reanalysis products using Universal Multifractals, *J. Hydrometeorol.*, *11*, 388–404, doi:10.1175/2009JHM1142.1.

Tessier, Y., S. Lovejoy, P. Hubert, D. Schertzer, and S. Pecknold (1996), Multifractal analysis and modeling of rainfall and river flows and scaling, causal transfer functions, *J. Geophys. Res.*, *101*, 26,427–26,440, doi:10.1029/96JD01799.

Vallis, G. (2010), Mechanisms of climate variability from years to decades, in *Stochastic Physics and Climate Modelling*, edited by P. W. T. Palmer, pp. 1–34, Cambridge Univ. Press, Cambridge, U. K.

Van der Hoven, I. (1957), Power spectrum of horizontal wind speed in the frequency range from 0.0007 to 900 cycles per hour, *J. Meteorol.*, *14*, 160–164, doi:10.1175/1520-0469(1957)014<0160:PSOHWS>2.0.CO;2.

Verrier, S., L. de Montera, L. Barthès, and C. Mallet (2010), Multifractal analysis of African monsoon rain fields, taking into account the zero rain-rate problem, *J. Hydrol.*, *389*(1-2), 111–120, doi:10.1016/j.jhydrol.2010.05.035.

Verrier, S., C. Mallet, and L. Barthès (2011), Multiscaling properties of rain in the time domain, taking into account rain support biases, *J. Geophys. Res.*, *116*, D20119, doi:10.1029/2011JD015719.

Vose, R. S., R. L. Schmoyer, P. M. Steurer, T. C. Peterson, R. Heim, T. R. Karl, and J. K. Eischeid (1992), The Global Historical Climatology Network: Long-term monthly temperature, precipitation, sea level pressure, and station pressure data, *Rep. ORNL/CDIAC-53, Environ. Sci. Div. Publ. 3912*, 325 pp., Oak Ridge Natl. Lab., Oak Ridge, Tenn., doi:10.3334/CDIAC/cli.ndp041.

Vose, R. S., K. Hilburn, X. Yin, M. Kruk, and A. Becker (2014), [Global climate] Precipitation [in ''State of the Climate in 2013''], *Bull. Am. Meteorol. Soc.*, *95*(7), S21–S22.